

Dielectrophoretic separation with a floating-electrode array embedded in microfabricated fluidic networks

Cite as: Phys. Fluids **30**, 112003 (2018); <https://doi.org/10.1063/1.5054800>

Submitted: 03 September 2018 . Accepted: 19 October 2018 . Published Online: 07 November 2018

Tianyi Jiang, Yukun Ren , Weiyu Liu, Dewei Tang, Ye Tao, Rui Xue, and Hongyuan Jiang



View Online



Export Citation



CrossMark

ARTICLES YOU MAY BE INTERESTED IN

[Theoretical analysis of non-linear Joule heating effects on an electroosmotic flow with patterned surface charges](#)

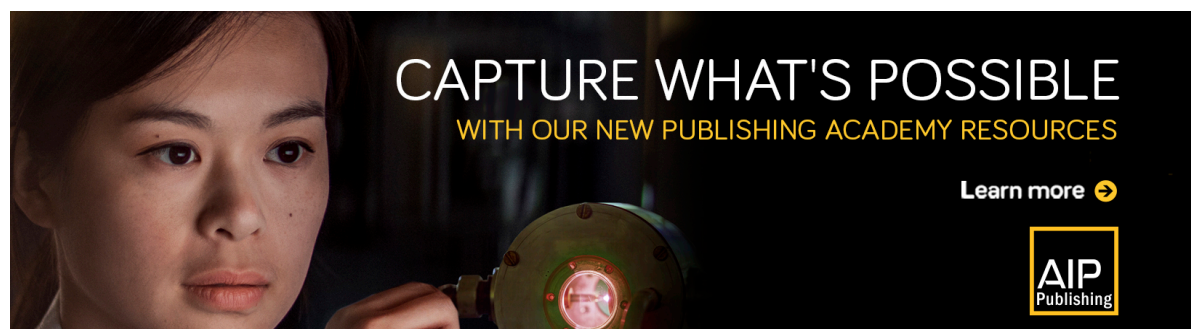
Phys. Fluids **30**, 112002 (2018); <https://doi.org/10.1063/1.5051175>

[Numerical investigation of electrowetting-based droplet splitting in closed digital microfluidic system: Dynamics, mode, and satellite droplet](#)

Phys. Fluids **30**, 112001 (2018); <https://doi.org/10.1063/1.5049511>



[Oil-water displacements in rough microchannels](#)

Phys. Fluids **30**, 112101 (2018); <https://doi.org/10.1063/1.5053625>



CAPTURE WHAT'S POSSIBLE
WITH OUR NEW PUBLISHING ACADEMY RESOURCES

Learn more 



Dielectrophoretic separation with a floating-electrode array embedded in microfabricated fluidic networks

Tianyi Jiang,¹ Yukun Ren,^{1,2,a)} Weiyu Liu,^{3,a)} Dewei Tang,¹ Ye Tao,¹ Rui Xue,¹ and Hongyuan Jiang^{1,a)}

¹State Key Laboratory of Robotics and System, Harbin Institute of Technology, West Da-Zhi Street 92, Harbin, Heilongjiang 150001, People's Republic of China

²The State Key Laboratory of Nonlinear Mechanics (LNM), Institute of Mechanics, Chinese Academy of Sciences, Beijing 100190, People's Republic of China

³School of Electronics and Control Engineering, Chang'an University, Middle-Section of Nan'er Huan Road, Xi'an, Shaanxi 710064, People's Republic of China

(Received 3 September 2018; accepted 19 October 2018; published online 7 November 2018)

In this study, we proposed a high-throughput separation strategy of the binary colloid mixture by dielectrophoresis (DEP) induced around large-scale bipolar electrode arrays embedded in microfabricated fluidic networks via a thorough numerical investigation. The usage of a floating electrode (FE) eliminates the need of external Ohmic connection to individual array units, therefore potentially steering the faddish design of new microdevice structures. Diffuse charge dynamics within the induced double layer at opposite ends of every FE permit a sinusoidal electric field to penetrate throughout the whole device, as long as the imposed field frequency is beyond the reciprocal resistor-capacitor time constant at the electrode/electrolyte interface. In this special device configuration, FEs interconnect multiple microchannels arranged in parallel. Pockets embedded on the sidewalls of fluidic channels help create strong field gradients at the tip of FEs and sharp pocket/channel junctions, improving the trapping performance of incoming bioparticles subjected to positive-DEP (pDEP) force, while latex beads experiencing negative-DEP (nDEP) stress are electrically squeezed to the midchannel and finally exit as a series of co-flowing thin streams with unequal translatory velocity. Taking the synergy of DEP force, induced-charge electro-osmosis, alternating-current electrothermal streaming, pressure-driven flow, and buoyancy effect into consideration, a numerical model is established to account for motion trajectories of micro-entities in full-scale three-dimensional space using the Lagrange particle track algorithm, as well as testing the feasibility of the device design in separation of the binary mixture containing yeast cells and polystyrene beads. Applying suitable voltage parameters of frequency $O(1)$ MHz and electric field strength $O(10)$ V/mm, highly efficient DEP separation is theoretically achievable under inlet flow velocity on the order of $O(1)$ mm/s, where most of incoming yeasts are captured by pDEP within these five parallel branching channels, while polystyrene spheres are repelled by nDEP away from the FE array to form slim beams co-flowing into the outlet according to the calculation results. The microfluidic separation device exploiting the FE array offers great potential to build up scalable electrokinetic platforms for high-throughput on-chip sample treatment. *Published by AIP Publishing.* <https://doi.org/10.1063/1.5054800>

NOMENCLATURE

DEP	dielectrophoretic
pDEP	positive dielectrophoretic
nDEP	negative dielectrophoretic
iDEP	insulator-based dielectrophoresis
TWDEP	traveling-wave dielectrophoresis
DE	driving electrode
FE	floating electrode
IDL	induced double layer
EDL	electrical double layer
ACEO	AC electroosmotic

ICEO	induced-charge electroosmotic
ACET	AC electrothermal
TWET	traveling-wave electrothermal
EHD	electrohydrodynamic
RHS	right-hand side
PS	polystyrene
PDMS	polydimethylsiloxane
RC	resistor-capacitor
DEs	driving electrodes
FEs	floating electrodes
AC	alternating current
DC	direct current

^{a)}Authors to whom correspondence should be addressed: rykhit@hit.edu.cn, Telephone: +86-0451-86418028, Fax.: +86-0451-86402658; liuweiyu@chd.edu.cn, Telephone: +86-029-82334543, Fax.: +86-029-82334555; and jhy_hit@hit.edu.cn, Telephone: +86-0451-86418028, Fax.: +86-0451-86402658.

Alphabetical symbols

C_D	diffuse layer capacitance (0.06 F m^{-2}) $C_D = \epsilon/\lambda_D$
C_S	stern layer capacitance (0.8 F m^{-2})

C_0	linear capacity of the entire electrical double layer (0.055 F m^{-2}) $C_0 = C_D/(1 + \delta)$
C_p	thermal capacity of water ($4200 \text{ J kg}^{-1} \text{ K}^{-1}$)
D	diffusion coefficient of ionic species ($2 \times 10^{-9} \text{ m}^2 \text{ s}^{-1}$)
E	electric field vector (V m^{-1})
E_t	tangential component of electric field vector (V m^{-1})
F_{external}	external force acting directly on particles freely suspended in saline solution (N)
f	field frequency (10 Hz-100 MHz)
f_{bulk}	charge relaxation frequency of fluid bulk (2.25 MHz) $f_{\text{bulk}} = \sigma/2\pi\epsilon$
f_{RC}	double-layer charge relaxation frequency (100-1000 Hz) $f_{RC} = \sigma(1 + \delta)/2\pi RC_D$
f_{ACET}	charge relaxation frequency of ACET flow (7.45 MHz) $f_{ACET} = \sigma\sqrt{1 - 2\beta/\alpha}/2\pi\epsilon$
H	height of the channel ($30 \mu\text{m}$)
K_S	surface conductivity of latex beads (1 nS)
k_f	thermal conductivity of suspension medium ($0.6 \text{ W m}^{-1} \text{ K}^{-1}$)
k_{PDMS}	thermal conductivity of PDMS channel walls ($0.2 \text{ W m}^{-1} \text{ K}^{-1}$)
k_{Glass}	thermal conductivity of glass substrate ($1 \text{ W m}^{-1} \text{ K}^{-1}$)
L	characteristic physical dimension ($100 \mu\text{m}$)
Pec	thermal Peclet number (0.07) $Pec = \rho_f C_p u L / k_f$
p	hydraulic pressure (Pa)
R	characteristic macroscopic length scale of double-layer capacitive charging (μm)
r	radius of latex beads ($2 \mu\text{m}$)
S	particle displacement vector (μm)
T	temperature field (K)
T_0	ambient temperature (293.15 K)
t	time elapsed (s)
u	characteristic flow velocity ($100 \mu\text{m s}^{-1}$)
u_f	flow velocity vector (m s^{-1})
u_p	particle velocity (m s^{-1})
u_0	inlet flow velocity (1 mm s^{-1})
V_D	voltage amplitude of the applied AC signal on DEs (30-60 V)
x	X coordinate (m)
y	Y coordinate (m)
z	suspension height of colloids away from the electrode surface (m)

Greek symbols

ϵ_f	liquid permittivity ($7.08 \times 10^{-10} \text{ F m}^{-1}$)
$\tilde{\epsilon}$	complex permittivity (F m^{-1}) $\tilde{\epsilon} = \epsilon - j\sigma/\omega$
σ_f	electrolyte conductivity (0.01 S m^{-1})
ϕ	electrostatic potential field (V)
α	thermal diffusivity of dielectric permittivity (-0.004 K^{-1}) $\alpha = \partial\epsilon/\partial T/\epsilon$
β	thermal diffusivity of liquid conductivity (0.022 K^{-1}) $\beta = \partial\sigma/\partial T/\sigma$
η	dynamic viscosity of water (0.001 Pa s^{-1})
ω	angular field frequency (rad s^{-1}) $\omega = 2\pi f$
ρ_f	mass density of water (1000 kg m^{-3})
ρ_p	mass density of incoming colloids (1050 kg m^{-3})

τ_{RC}	double-layer charge relaxation time (s) $\tau_{RC} = RC_D/\sigma(1 + \delta)$
δ	surface capacitance ratio (0.074) $\delta = C_D/C_S$
ζ	induced zeta potential on ideally polarizable surfaces (V) $\zeta = \text{Re}((\tilde{\phi}_E - \tilde{\phi})e^{j\omega t})/(1 + \delta)$
ϕ_E	the body potential of DE and FE (V)
λ_D	Debye screening length (12 nm) $\lambda_D = \sqrt{D\epsilon/\sigma}$

Subscripts

ACET	AC electrothermal
B	background
bulk	fluid bulk
CM	C-M factor
D	diffuse layer
DE	driving electrode
E	electrode
FE	floating electrode
f	working fluid
Glass	glass substrate
MW	Maxwell-Wagner
PDMS	polydimethylsiloxane
p	particle
S	stern layer
t	tangential component

Superscripts

*	complex conjugate operator
RC	resistor capacitor

Mathematical symbols

$\langle A \rangle$	time-average operation
\tilde{A}	phasor amplitude
$\text{Re}(A)$	real part operator

I. INTRODUCTION

Separation of inorganic colloids and biological cells at micrometer dimension is important to broad on-chip applications, such as water quality monitoring,¹ early cancer diagnosis,² intercellular communication investigation,³ biomedical assay,⁴ and so on. Among a diversity of available microfluidic separation techniques, including viscoelastic effect,⁵ Rayleigh streaming,⁶ magnetic manipulation,⁷ diffusiophoresis,⁸⁻¹⁰ and electrokinetic phenomena,¹¹⁻¹⁸ dielectrophoresis (DEP) provides a mild and promising separation way to insulate particle samples according to difference in their dielectric properties.¹⁹⁻²⁴

DEP arises from an externally applied uneven direct-current (DC)/alternating-current (AC) electric field interacting with polarizable dielectric colloids.²⁵ If the polarizability of particles is lower than that of the liquid suspension, they will be repelled away from electrode surfaces to regions of lower field strength, i.e., negative-DEP (nDEP). On the other hand, once they are more polarizable, colloids will be attracted by the voltage source and move in the direction of increasing field gradients, namely, positive-DEP (pDEP). Since particle polarizability relative to the suspension medium is determined by

a delicate combination of transient conduction and displacement currents, there is a sensitive frequency dependence for DEP response of leaky dielectric beads in AC fields.

For colloids with higher (lower) conductivity but lower (higher) permittivity than that of the liquid suspension, pDEP (nDEP) and nDEP (pDEP) appear at low and high field frequencies, respectively. So, there is always one critical frequency across which in-phase induced polarization transits from a low-frequency conductivity plateau to a high-frequency permittivity plateau, while the out-of-phase counterpart attains a relaxation peak [traveling-wave dielectrophoresis (TWDEP)] around.^{26,27} As to biological cells with compound core-shell structures, Maxwell-Wagner interfacial polarization is made more complicated by those intracellular sharp material interfaces, and as a result, there will be more than one transition frequency in DEP response to harmonic excitations, with the specific number depending on the living state of cells.

To achieve continuous isolation of latex beads and bioparticles at a given ionic strength of the background electrolyte, a suitable range of electric field frequencies has to be found so that the two types of particles experience DEP force in reverse directions, which makes it a great challenge to

separate the binary liquid mixture containing colloidal and cellular particles. For such, a lot of microfluidic devices have been developed to employ DEP for sorting micro/nanofluidic samples successfully.^{28–30} Conventionally, researchers make use of ideally polarizable microelectrode arrays embedded in microfluidic channels, so as to generate the strong field gradient required for DEP operation.³¹ However, in electrokinetic chips with planar electrodes, the actuating range of DEP force is severely confined to the immediate vicinity of conducting surfaces, resulting in poor separation performance and throughput. An already-existing cost-effective approach to extend the DEP force field is to take advantage of insulating obstacles disposed in fluidic channels, redistributing the electric field around the hurdles with local field maximum produced at the poles, namely, the insulator-based DEP³² (iDEP). From the previous literature, it can be inferred that insulating barriers are in favor of integrating with distinct electrode features, thereby enabling novel device designs possessing multiple functionalities.³³

In this study, we propose an alternative method to enhance the separation flux of a DEP device. Our chip (Fig. 1) utilizes an array of floating electrodes (FEs) for high-throughput

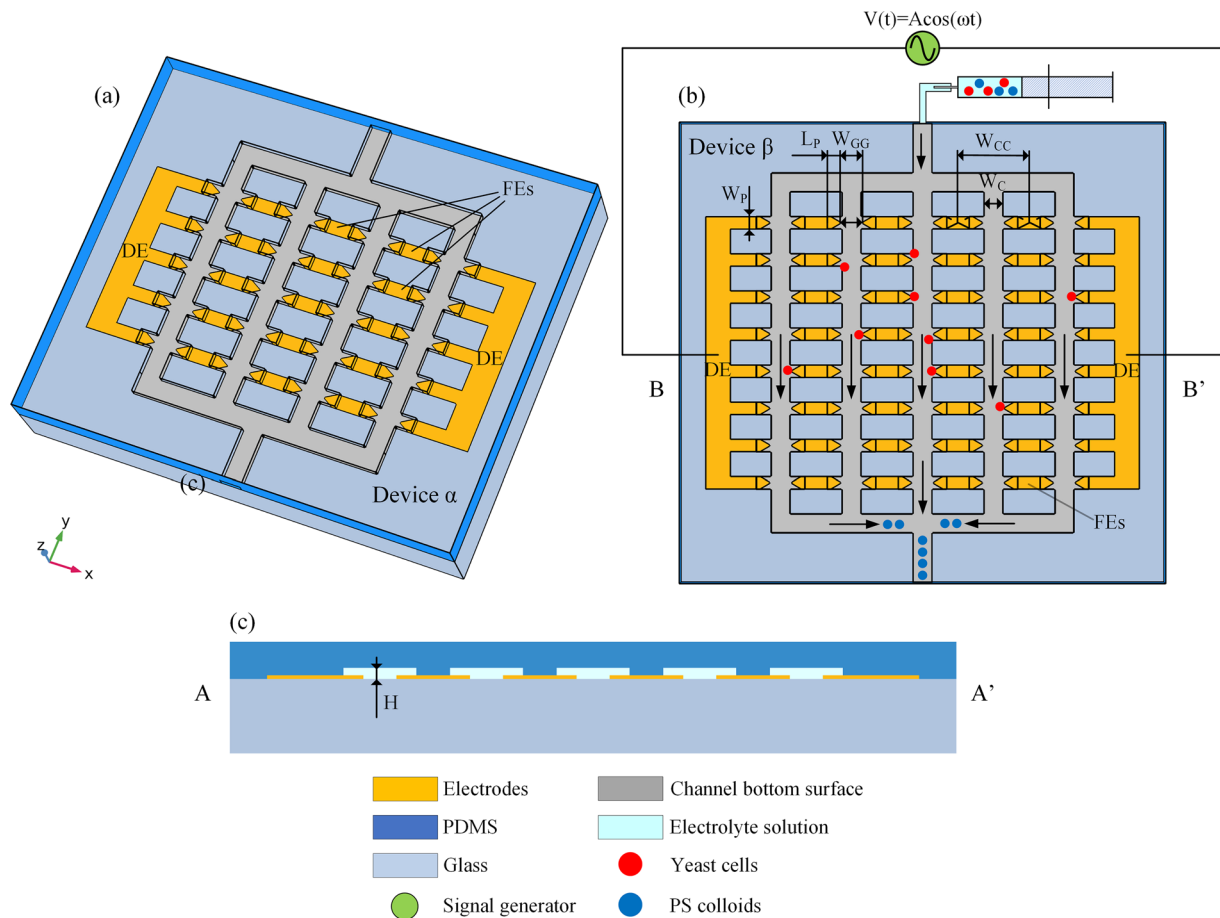


FIG. 1. A schematic representation of the microfluidic separation device by exploiting DEP force fields induced by a large-scale FE array. (a) A 3D view of a microfluidic network with 4 branching channels sharing a single inlet and outlet, in which a 3×5 FE array is embedded beneath insulating channel walls with the two opposite ends of the individual array element immersed in the buffer solution so that an AC electric field emitted from the DE on both sides can be transmitted across the electrolyte solution within each fluidic channel by double-layer capacitive charging at the ideally polarizable surfaces (device α). (b) Top view of one highly integrated device design (device β) with a 4×8 FE array for high-throughput electrokinetic separation of incoming yeast cells (pDEP) and latex beads (nDEP), in an x - y plane at a vertical distance $z = 3 \mu\text{m}$ away from the electrode surface (the B-B' cross section). (c) Side view of the proposed microdevice in an x - z plane connecting all the electrode tips (the A-A' cross section). The physical size labeled in (b) is explicitly presented in Table I.

isolation of the binary colloid mixture of inorganic polystyrene (PS) beads and biological yeast cells based upon the difference in their electrical polarizabilities. Importantly, the highly integrated bipolar FE array transmits a sinusoidal electric field across a series of insulating obstacles [polydimethylsiloxane (PDMS) channel sidewalls] by capacitive charging of the induced double-layer (IDL) at the FE/electrolyte interface, therefore allowing simultaneous trapping of yeast cells within multiple separation channels configured in parallel. Rectangular micro-pockets oriented in the direction of FE tips and disposed along the insulating sidewalls of each branching channels offer a number of discrete capture locations adjacent to the sharp corner-field-singularity at pocket/channel junctions as well as the conducting surfaces of floating electrodes (FEs), giving rise to stable immobilization of yeast cells subjected to a pDEP force field. Bipolar FEs exempt from external powering are of great significance to the current microfluidic separation scheme using parallel branching microchannels. Considering a coexistence of Debye screening,^{34–36} induced-charge electroosmosis^{37–41} (ICEO), AC electrothermal^{42–46} (ACET) streaming, in-phase DEP force,³¹ and gravitational sedimentation,^{47,48} a numerical model is developed, where the Lagrange particle track algorithm is used to trace motion trajectories of the incoming bead mixture in full-scale three-dimensional space, demonstrating the importance of the DEP effect in successfully isolating yeast cells from interfering PS colloids in the frequency range that it dominates. The key feature that distinguishes the method reported here from previous approaches is that it can generate high-throughput at almost no cost of sacrificing the separation performance. The advantages of this method, such as high flow flux, ease of integration, and gentle operating condition, make it a superior candidate in applications of early stage cancer diagnosis, water quality monitoring, chemistry sample preparation, transesterification of microalgal lipid to biodiesel, and so on.

II. MATERIALS AND METHOD

A. Device design

As shown in Fig. 1, to construct a microfluidic DEP device that can separate the binary colloid mixture at high-throughput, we present herein two structural designs, including the basic architecture of 4 parallel branching channels for an in-depth study of the fundamental working principle of the current DEP separation device in static condition [Fig. 1(a)] and a highly integrated microfluidic network of 5 branching channels for continuous separation under dynamic situation [Fig. 1(b)], with specific geometric dimensions indicated in Figs. 1(b) and 1(c) and Table I.

4 (or 5) branching channels with each one being 0.85 mm (or 1.3 mm) long \times 76 μm wide \times 30 μm tall are configured

in parallel with a center-to-center distance of 0.286 mm. Each fluidic channel has 5 (or 8) pockets embedded at either side (a total of 40 or 80 pockets). Each pocket is of 60 μm in length and 50 μm in width and the edge-to-edge distance of two adjacent pockets was 88 μm . All microchannels are in connection to a common entrance and exit for convenience of integration with other micro/nanofluidic components. The FEs stretch into the pockets from the bottom of PDMS to an axial distance of 6 μm away from the straight channel. The devices are designed to operate such that the leaky dielectric beads suspended in conducting buffer solution would flow through the fluidic networks and become either trapped at the tips of FEs by pDEP attraction or maintained in the laminar streams by nDEP repulsion [Fig. 1(b)]. The microfluidic DEP device is finally accomplished by rendering the coplanar driving electrodes (DEs) oppositely polarized upon application of a sinusoidal signal to the contact pads on both sides of the central FE array.

Considering the feasibility of experimental implementation, we presented herein a possible method for fabricating the electrokinetic microdevice as follows:

- (a) For processing the microelectrode array: First, indium-tin-oxide (ITO) glass slides (one side of them was covered by thin film ITO) were spin-coated with a kind of positive photoresist (AZ 4620); second, the slides were exposed to ultraviolet (UV) light through a mask onto which the electrode structure was printed for transferring the pattern; third, a developing solution (ZX-238) and hydrochloric acid were employed to etch the electrodes' pattern, and finally the slides were immersed in acetone to dissolve any remaining photoresist.
- (b) The microchannel was fabricated by the soft lithography technique: First, similar to the exposure process of ITO glass slides, glass slides were manually attached by several layers of dry film (SD238) and then exposed to UV light through a photomask onto which the pattern of channels was painted; second, bicarbonate and aluminum foil were used to dissolve the redundant dry film and form a mold for subsequent polymerization; third, a PDMS precursor was poured into the mold and cured at 80 °C for 2 h to develop the channel.
- (c) Finally, the glass substrate with desired electrode patterns and insulating PDMS channel were carefully aligned under a microscope and reversibly bonded together by O₂ plasma treatment.

B. Theory

A FE is referred to as a metal conductor in an ionic electrolyte.^{49–51} When subjected to an externally applied DC/AC electric field, it can facilitate the capacitive charging of induced double layer (IDL) simultaneously on opposite ends of the ideally polarizable surface of FE. For instance, a FE may consist of a metal strip deposited in a microchannel stuffed with saline solution. When a DC potential bias is imposed across the chamber, a linear potential gradient is anticipated along the channel length direction due to the high impedance of fluid bulk with respect to that of conducting probes. The uniform electric field distribution gives rise to potential drops between the bipolar

TABLE I. The specific geometry size indicated in Fig. 1(b).

Parameter	W_C	W_P	W_{GG}	W_{GG}	L_P	L_C	H
Value (μm)	76	50	88	286	60	1300	30

FE and the solution in direct contact with its surface. After a characteristic resistor-capacitor (RC) charge relaxation time, an IDL of bipolar counterions is formed at each end of FE.^{52–54} Under this situation, the electric current runs between the DEs either via electromigration of ionic species in electrolyte solution or through the FE array by double-layer capacitive charging with severe electrochemical reactions.

Nevertheless, when an AC voltage wave of sufficiently high field frequency is utilized to excite the microsystem rather than a static DC potential difference, Faradaic current injection does not take place any longer due to electrochemical ion relaxation. Moreover, once the bottom of the fluidic channel touches directly the surface of FE [Fig. 1(c)], then the probability of ionic conduction on top of the FE array is eliminated. Under this situation, incessant charging and discharging of IDL induced between each end of a FE and the liquid suspension is the main path through which the AC voltage wave drives the ionic current flow between the pair of driving electrodes (DEs).

At field frequencies beyond the reciprocal RC time constant f_{RC} for the equivalent circuit of IDL capacitor in series connection with resistance of fluid bulk, incomplete AC-field-induced Debye screening on FEs would make these parallel branching channels electrically interconnected. Since all the FEs are ideal conductors of equipotential quality, each of them takes on a harmonic potential that is in the midst of the potential value of the liquid bulk at its both ends. In this way, the electric field is transmitted throughout the entire system in each separation channel, generating DEP force fields that are sufficiently potent to isolate the binary colloid mixture of opposite DEP polarity in continuous pressure-driven flows [Fig. 1(b)]. Besides, the electric field is flexibly reconfigurable by adjusting the dimension of FE. For example, triangular FEs induce a local field maximum at the electrode tips, while the field intensity attains a minimum in the midchannel. In this sense, FEs not only transfer the AC electric field across the microdevice but on-demand reshape the profile of potential gradient as well.

C. Mathematical formulation

1. Electrode polarization and induced-charge electroosmosis

Since we make use of the point-dipole approach to evaluate the time-averaged DEP force in AC fields, the volume of liquid occupied by freely suspended particles would not impose any effect on various field variables in the microfluidic system. As for the problem of quasi-electrostatics, the entire system can be divided into two interconnected regions, including the liquid suspension and IDL at the electrode/electrolyte interface. Within the former, the ion conductivity is homogeneous to the first order. So, charge conservation is governed by the Laplace equation. For convenience of mathematical analysis, we take advantage of the complex amplitude under the approximation of harmonic actuation and linear response, e.g., the transient sinusoidal potential $\phi(t)$ in the time domain can be expressed in terms of voltage phasor $\tilde{\phi}$ with a tilde symbol in frequency domain, i.e., $\phi(t) = \text{Re}(\tilde{\phi}e^{j\omega t})$. To this end, the current continuity condition within the buffer solution is

reduced to

$$\nabla^2 \tilde{\phi} = 0. \quad (1)$$

Using the Debye-Huckel approximation, we disregard those detrimental effects that may cause damage to electrode structures, including redox reaction, ion overcrowding, concentration polarization, and so on. The IDL, which is formed between either end of the FE and the electrolyte solution in touch with it, is comprised of an immobile Stern layer of capacitance C_S and a mobile diffuse layer of capacitance $C_D = \varepsilon_f/\lambda_D$, both of which are connected in sequence to support the entire potential drop across the ideally polarizable interfaces. Here, λ_D denotes the Debye screening length and ε_f denotes the solution permittivity. So, the total linear capacity of IDL results from a combination of these two distinct thin layers, i.e., $C_0 = C_D C_S / (C_D + C_S) = C_D / (1 + \delta)$, with a surface impedance ratio of $\delta = C_D / C_S$. Since the ideally polarizable surface of the blocking electrode forbids any normal motion of charge carriers within the thin IDL, it should be satisfied at the outer edge of the diffuse screening cloud that the conduction current from the fluid bulk is continuous with the displacement current flowing across the Debye layer,²⁷

$$\sigma_f \mathbf{n} \cdot \nabla \tilde{\phi} = j\omega \frac{C_D}{1 + \delta} (\tilde{\phi} - \tilde{\phi}_E), \quad (2)$$

where σ_f is the fluid conductivity, $\tilde{\phi}$ is the complex potential in the bulk right outside the IDL, $\tilde{\phi}_E$ is the voltage amplitude of either DE or FE, $\omega = 2\pi f$ is the angular field frequency, and \mathbf{n} is the unit vector normal to the conducting surface. It is presumed that the only way to short circuit IDL is through the polarization current in high-frequency AC electric fields. We do not have to analyze the internal structure of IDL and, instead, interfacial impedance is described by a Robin-type boundary condition, Eq. (2). A dimensional analysis of Eq. (2) results in a typical RC relaxation frequency $f_{RC} = (1 + \delta)\sigma_f \lambda_D / 2\pi \varepsilon_f R = O(1-10)$ kHz for dilute electrolytes in microsystems, with R being the macroscopic distance scale of electrode polarization, e.g., $R = L_F$ for ICEO on FE and $R = n \cdot W_C$ for AC electroosmosis (ACEO) on DE. After substitution, $f_{FE}^{RC} = (1 + \delta)\sigma_f \lambda_D / 2\pi \varepsilon_f L_F$ and $f_{DE}^{RC} = (1 + \delta)\sigma_f \lambda_D / 2\pi \varepsilon_f n W_C$. Here, L_F denotes the length of a section of FE whose conducting surface is in contact with the buffer medium, and n is the number of branching channels. Because $n \cdot W_C$ is much larger than L_F , f_{DE}^{RC} is invariably no more than f_{FE}^{RC} in our device design.

The complex amplitude of the induced zeta potential that drops across the diffuse layer of mobile counterionic charges is given by³⁵

$$\tilde{\zeta} = \frac{1}{1 + \delta} (\tilde{\phi}_E - \tilde{\phi}). \quad (3)$$

Coulomb force within the thin IDL gives rise to steady ICEO slipping on the electrode surface subjected to a tangential field component $\mathbf{E}_t = \text{Re}(\tilde{\mathbf{E}}_t e^{j\omega t}) = \text{Re}((\tilde{\mathbf{E}} - \tilde{\mathbf{E}} \cdot \mathbf{n} \cdot \mathbf{n})e^{j\omega t})$,

$$\mathbf{u}_{slip}(t) = -\frac{\varepsilon \zeta}{\eta} \mathbf{E}_t = -\frac{\varepsilon}{\eta} \text{Re}(\tilde{\zeta} e^{j\omega t}) \text{Re}((\tilde{\mathbf{E}} - \tilde{\mathbf{E}} \cdot \mathbf{n} \cdot \mathbf{n})e^{j\omega t}), \quad (4)$$

where η is the dynamic viscosity of the liquid suspension.

For convenience of theoretical analysis, the time-averaged counterpart of Eq. (4) is utilized for calculating ICEO vortex flow field,

$$\begin{aligned} \langle \mathbf{u}_{slip}(t) \rangle &= -\frac{\varepsilon}{2\eta} \text{Re} \left(\tilde{\zeta} \cdot (\tilde{\mathbf{E}} - \tilde{\mathbf{E}} \cdot \mathbf{n} \cdot \mathbf{n})^* \right) \\ &= \frac{\varepsilon}{2\eta(1+\delta)} \text{Re} \left((\tilde{\phi}_E - \tilde{\phi}) \cdot (\nabla \tilde{\phi} - \nabla \tilde{\phi} \cdot \mathbf{n} \cdot \mathbf{n})^* \right), \end{aligned} \quad (5)$$

where $\langle A \rangle$ denotes the time-average of A , $\text{Re}(A)$ denotes the real part of a complex number A , and an asterisk $*$ denotes the complex conjugate operator.

2. Electrothermal induced flow

Different from ICEO surface slipping originated by external-field-driven diffuse charge dynamics, ACET appears as bulk electro-convective streaming due to Maxwell-Wagner structural polarization, and dominates at higher field frequencies. Since material electrical properties usually vary with local temperatures, electric heat generation would lead to anisotropic distribution of liquid conductivity and dielectric permittivity inside the bulk fluid. For the Gauss law and charge conservation equation to be satisfied simultaneously, both free and polarized bound charges have to be induced by the interplay of such dielectric gradients with the applied electric field, which is also responsible for DEP force acting on the liquid volume. So, just like ICEO, ACET belongs to a category of nonlinear electrohydrodynamic (EHD) flow as well and thereby exists well in AC fields. Using a linear perturbation analysis, the time-averaged AC electrothermal body force acting on each liquid unit was obtained by Ramos *et al.*,⁴⁸

$$\langle \mathbf{f} \rangle = \frac{1}{2} \varepsilon_f \text{Re} \left(\frac{(\alpha - \beta)}{1 + j\omega\tau_{MW}} \nabla T \cdot \tilde{\mathbf{E}} \cdot \tilde{\mathbf{E}}^* - \frac{1}{2} \alpha (\tilde{\mathbf{E}} \cdot \tilde{\mathbf{E}}^*) \nabla T \right), \quad (6)$$

where $\tau_{MW} = \frac{\varepsilon_f}{\sigma_f}$ denotes charge relaxation time of the bulk suspension. $\alpha = \frac{\partial \varepsilon_f}{\partial T} / \varepsilon_f = -0.004/\text{K}$ and $\beta = \frac{\partial \sigma_f}{\partial T} / \sigma_f = 0.022/\text{K}$ are thermal diffusivities of liquid permittivity and conductivity, respectively. The two sequential terms on the right-hand side (RHS) of Eq. (6) represent the Coulomb force due to the induced free charge and dielectric force acting on the polarized bound charge, respectively. The Coulomb force dominates at low frequencies, while only dielectric force can survive in the high-frequency limit considering a charge relaxation process. The two distinct force components act in opposite directions and counterbalance one another at a critical field frequency $f_{ACET} = \sigma_f \sqrt{1 - 2\beta/\alpha} / 2\pi\varepsilon_f$, which is about $\sqrt{11}$ times the reciprocal of bulk charge relaxation time $f_{MW} = \sigma_f / 2\pi\varepsilon_f$, and both of them are orders of magnitude higher than the inverse RC time constant including $f_{DE}^{RC} = (1 + \delta)\sigma_f\lambda_D / 2\pi\varepsilon_f n W_C$ and $f_{FE}^{RC} = (1 + \delta)\sigma_f\lambda_D / 2\pi\varepsilon_f L_F$.

The energy balance equation with a Joule heating source is solved within the entire microsystem, including the fluid domain, PDMS walls, and glass substrate,⁵⁵

$$\nabla \cdot (k_f \nabla T) + \frac{1}{2} \sigma_f (\tilde{\mathbf{E}} \cdot \tilde{\mathbf{E}}^*) = 0 \quad (\text{in suspension medium}), \quad (7a)$$

$$\nabla^2 T = 0 \quad (\text{in PDMS walls and glass substrate}), \quad (7b)$$

where $k_f = 0.6 \text{ W/(m K)}$ is the thermal conductivity of the buffer solution. It is worth to note that the thermal Peclet number $\text{Pec} = \rho_f C_p u L / k_f$ characterizes to which extent the flow field plays a major role in smoothing the temperature rise inside the liquid phase. Here, $\rho_f = 1000 \text{ kg/m}^3$ denotes the liquid mass density, $C_p = 4200 \text{ [J/(kg K)]}$ denotes the thermal capacity of water, u denotes the characteristic flow velocity, and L denotes the physical dimension (see the Nomenclature). In typical microsystems with $u = 100 \text{ }\mu\text{m/s}$ and $L = 100 \text{ }\mu\text{m}$, $\text{Pec} = 0.07$ is even less than a unit, which indicates that thermal convection in a fluid flow can be safely ignored in comparison with the effect of Fourier heat conduction for Eq. (7a). In this way, a decreasing EHD flow velocity at higher field frequencies does not impose an important effect on the temperature elevation from electric heat generation within a channel.

The DEP force density Eq. (6) is inserted into the full Stokes equation as a source term of electrical origin, so as to acquire the ACET vortex flow field above the conducting surface,

$$\begin{aligned} -\nabla p + \eta \nabla^2 \mathbf{u}_f + \frac{1}{2} \varepsilon_f \text{Re} \left(\frac{(\alpha - \beta)}{1 + j\omega\tau_{MW}} \nabla T \cdot \tilde{\mathbf{E}} \cdot \tilde{\mathbf{E}}^* \right. \\ \left. - \frac{1}{2} \alpha (\tilde{\mathbf{E}} \cdot \tilde{\mathbf{E}}^*) \nabla T \right) = 0, \end{aligned} \quad (8a)$$

$$\nabla \cdot \mathbf{u}_f = 0, \quad (8b)$$

where p denotes the hydraulic pressure and $\mathbf{u}_f = (u_x, u_y, u_z)$ denotes the flow field.

3. Dielectrophoresis

For an individual colloid immersed in saline solution, it would undergo Maxwell-Wagner interfacial polarization during exposure to an externally applied DC/AC electric field. If there is a difference in electrical polarizability between the particle and suspension medium, both free and bound charge have to be induced at the surface of the solid colloid by the applied field in order to insure the continuity of the normal component of the total current density across the sharp material interface. In a non-uniform electric field, the electric stress acting on the bipolar surface charge would give rise to a net particle DEP motion. The macroscopic DEP force due to interfacial charge relaxation causes particle samples of higher (lower) polarizability than that of the medium to move to strong (weak) electric field regions, so as to maximize the system electrical energy. For a spherical colloid of radius r , the time-averaged in-phase component of this ponderomotive electrostatic force in harmonic fields is predictable by the point-dipole theory,

$$\langle \mathbf{F}_{DEP} \rangle = \pi \varepsilon_f r^3 \text{Re}(f_{CM}(\omega)) \nabla (\tilde{\mathbf{E}} \cdot \tilde{\mathbf{E}}^*). \quad (9)$$

The DEP force field depends sensitively on the exciting frequency via either the complex Clausius-Mossotti (C-M) factor $f_{CM}(\omega) = \frac{\tilde{\varepsilon}_p - \tilde{\varepsilon}_f}{\tilde{\varepsilon}_p + 2\tilde{\varepsilon}_f}$ or the electric field distribution \mathbf{E} . Here, $\tilde{\varepsilon}_p = \varepsilon_p - j \frac{\sigma_p}{\omega}$, ε_p , and σ_p stand for the complex permittivity, real dielectric permittivity, and electrical conductivity, respectively, where the subscript ‘‘p’’ indicates the particle and j indicates the imaginary unit. Likewise, the corresponding dielectric properties for the liquid suspension are signified by the subscript ‘‘f.’’ The real part of induced polarizability $\text{Re}(f_{CM}(\omega))$ ranging from -0.5 to 1 for a spherical

entity regulates the direction of DEP force, which can either be positive (colloids are attracted toward field maxima and is named pDEP) or negative (particles are repelled away from the electrode surface to weak field regions and is termed nDEP).

Considering non-uniform surface electrokinetic transport on a curved interface,⁵⁶ the conductivity of a solid particle of spherical shape is given by

$$\sigma_p = \sigma_p^{bulk} + 2K_S/r, \quad (10)$$

where σ_p^{bulk} denotes the bulk conductivity of a weakly polarizable particle on the order of 10^{-16} S/m and K_S denotes the surface conductance equaling 10^{-9} S for colloids with diameter no less than $1 \mu\text{m}$. On the other hand, as shown in Table II, in-phase polarizability of bioparticles such as yeast cells can be calculated via modeling these cell particles as microspheres comprising of three concentric layers with distinct values of permittivity and conductivity.^{57,58}

4. Particle dynamics

Considering negligibly small inertial effects in typical microsystems, the velocity of incoming particles \mathbf{u}_p can be treated as a high-fidelity measure of the flow field \mathbf{u} plus the movement due to any external force acting directly on it,⁴⁷

$$\mathbf{u}_p = \mathbf{u}_f + \frac{F_{external}}{6\pi\eta r} = \mathbf{u}_{laminar} + \mathbf{u}_{ICEO} + \mathbf{u}_{ACET} + \frac{\langle F_{DEP} \rangle}{6\pi\eta r} + \frac{F_{buoyancy}}{6\pi\eta r}, \quad (11)$$

where the five terms on the RHS of Eq. (11) denote in sequence the fluidic drag due to the axial incoming laminar stream, ICEO and electrothermal convective rolls in the transverse direction, particle DEP velocity, and gravity sedimentation considering the downward buoyancy force $\mathbf{F}_{buoyancy} = -(\rho_p - \rho_f)V_p g \mathbf{e}_z$. Here, ρ is the mass density of particle (p) or fluid (f), $V_p = 4\pi r^3/3$ is the particle volume, and g is the gravitational acceleration.

Considering trivial Brownian diffusion of microscale entities, their motion trajectory $\mathbf{s} = (x, y, z)$ is governed by the kinematic equation

$$\frac{d\mathbf{s}}{dt} = \mathbf{u}_p. \quad (12)$$

TABLE II. Geometrical and electrical properties of the spherical yeast cells comprising of three concentric layers as well as the latex beads used in numerical modeling.

Property	Value		
	Wall	Cytoplasm	Nucleus
Yeast cell			
Radius (μm)	2.5	2.36	2.35
Conductivity ($\mu\text{S/cm}$)	140	0.0025	2000
Relative permittivity	60	6	50
Polystyrene particle			
Radius (μm)	2		
Bulk conductivity ($\mu\text{S/cm}$)	0		
Relative permittivity	2.55		
Surface conductance (nS)	1		

D. Numerical simulation

A commercial finite-element-modeling-based software package, Comsol Multiphysics (version 5.2), is employed to analyze the effect of various electrokinetic phenomena on dynamic behaviors of the incoming binary colloid mixture and resulted separation performance. As mentioned above, four types of nonlinear electrokinetics, including electrochemical polarization, ICEO, ACET, and DEP, coexist in the microdevice and they interplay actively within a broad frequency range from below the inverse RC time constant $f_{DE}^{RC} = (1 + \delta)\sigma_f \lambda_D / 2\pi\epsilon_f n W_C$ to beyond bulk charge relaxation frequency $f_{ACET} = \sigma_f \sqrt{1 - 2\beta/\alpha} / 2\pi\epsilon_f$.

The simulation procedure of DEP-based particle separation is as follows:

- First, we compute the Laplace equation Eq. (1) to get the AC potential field within the liquid suspension, which is subjected to the RC charging condition Eq. (2) at the medium/electrode interface. The bulk potential of the driving electrode (DE) pair equals V_D and 0 on either side of the FE array, respectively, while that of each array element is determined implicitly by charge conservation. Besides, other insulating interfaces are assumed to inhibit any normal current flux, i.e., $\mathbf{n} \cdot \nabla \phi = 0$, and consequently, the basic feature of electrochemical ion relaxation under sinusoidal steady state is correctly captured by numerical modeling.
- Next, Eq. (7) for diffusive heat transfer is calculated within the whole microsystem, including the patterned PDMS lid, fluid compartments, and glass substrate, where we have considered coupling between electric and thermal fields via inserting the source term of Joule medium heating into Eq. (7a). The conjugating condition of temperature and normal thermal flux is applied at the PDMS/medium interface as well as the substrate surface. The specific thermal conductivity of the PDMS cover and glass base is $k_{PDMS} = 0.2$ W/(m K) and $k_{Glass} = 1$ W/(m K), respectively. Room temperature $T_0 = 293.15$ K is imposed on top of the PDMS lid and bottom of the insulating substrate. All other boundaries are assumed to be adiabatic, i.e., $\mathbf{n} \cdot \nabla T = 0$. Simultaneously, the DEP force field exerted on different particle species can be calculated by using corresponding dielectric properties and a common distribution of the electric field gradient.
- Once the potential and temperature distribution are known, it is then possible to calculate the full Stokes equation Eq. (8) for getting the synthetic flow field within the branching channels, including the longitudinal Poiseuille flow caused by an externally applied hydrodynamic pressure difference, ACET and ICEO electro-convective streaming on application of an AC signal: an averaged flow rate u_0 is designated at the channel inlet, and hydraulic pressure reaches zero at the channel outlet, so as to imitate the pressure-driven flow for continuous injection of the binary colloid mixture; simulation of ACET fluid motion is achieved by a force density approach;⁵⁹ emergence of ICEO whirlpools is reflected by inserting the time-averaged electrokinetic

slip velocity Eq. (5) as a moving-wall boundary condition on the ideally polarizable surface of all of the blocking electrodes, including the DE pair and central FE array. In addition, other non-polarizable interfaces are subjected to physical constraints of no slip and no penetration.

- (d) Finally, according to Eq. (11), by stacking up the axial laminar streams, lateral EHD whirlpools, DEP force, and gravitational sedimentation, the resultant velocity field of incoming particle species is obtained, which depends sensitively on the applied field frequency in terms of bipolar electrochemistry and Maxwell-Wagner interfacial polarization. Accordingly, by conducting the time integral of the synthetic velocity field, yeast cells and PS beads may exhibit distinct motion trajectories within the microfabricated fluidic networks as they are transported downstream, which has the potential to help separate the incoming binary colloid mixture successfully.

The full-scale three-dimensional AC electric field, thermal conduction, and fluid physics are solved in sequence using stationary solvers, with grid-independence checked carefully for each simulation result. The maximum grid size in the vicinity of the electrode surface is designated to be no more than one-twentieth of the width of an individual metal electrode. Especially, the mesh distribution is quite refined right at the electrode tips and sharp channel corners. This meshing scheme leads to 4 049 677 tetrahedra in the three-dimensional calculation space. Any further refinement of grid partitioning will make the simulation result deviate from the current condition by less than 5%. We make use of a transient solver to resolve the spatio-temporal evolution of physical displacement of colloidal particles from a massless kinematic equation, in which 100 yeast cells and PS microspheres are repeatedly released from the channel entrance at the same time with a definite interval of 0.05 s. The total time period of numerical calculation lasts for 30 s, where all the samples subjected to nDEP force are directed to the channel outlet manifesting as multiple co-flowing thin streams. To guarantee the simulation accuracy, the maximum time step of computation is stipulated to be no more than 0.004 s in the settings of the time-dependent solver.

III. RESULTS AND DISCUSSION

A. Effect of various nonlinear electrokinetic phenomena

1. Maxwell-Wagner interfacial polarization

The main principle responsible for particle separation in the presented microfluidic device is dielectrophoresis. In principle, under the influence of a DC/AC electric field supplied from the driving electrodes, considering the mismatching dielectric properties between the colloids and suspension medium, electric field has to be discontinuous across the sharp material interface in order to ensure the continuity of total current density (conduction plus displacement). Then, according to the surface form of the Gauss law, a local charge density distribution, including both free and bound charge, has to be

induced by the applied field itself at the particle surface of a sharp gradient in conductivity and permittivity. This physical phenomenon capable of induction of a surface charge wave is termed as Maxwell-Wagner interfacial polarization.⁶⁰ An action of the electric field on its own induced charge can generate a time-averaged component of electrokinetic force even under AC forcing, in that both of them oscillate at the same exciting frequency which results in a non-zero product value within every oscillation period.

As a matter of fact, DEP due to interfacial charge relaxation was most initially proposed by Melcher⁶¹ to transport fluids in a traveling potential wave at the interfacial relaxation frequency, where a liquid conductivity gradient vertical to the level of the electrode array is required, as provided by two thin fluid layers coflowing along the channel length direction. Out-of-phase electrical stress acting on the two-phase contact interface of a traveling wave of induced surface charge actively pumps the buffer solution either in or against the direction of signal-phase propagation within an intermediate frequency range, as determined by the specific direction of variation of conductivity. Later, Pohl⁶² demonstrated the existence of in-phase effect of DC/AC DEP, which moves particles of higher (or lower) polarizability suspended in another medium in the direction of increasing (or decreasing) electric field strength. In-phase DEP force components can be merely induced by a non-uniform electric field (either DC or AC due to its nonlinear trait), trying to render the system electrical energy maximized. Following the pioneering work of Melcher⁶¹ and Pohl,⁶² Wang and co-workers⁶³ derived general expressions of DEP force for leaky dielectric particles freely suspended in conductive liquid suspension from first principles using the Maxwell stress tensor approach, where a series of progressively phase-shifted AC voltage signals are imposed on a linear electrode track disposed along the channel bottom surface. It was discovered by their analytical solution that, with the increase of field frequency, an increasing (decreasing) in-phase polarizability is always accompanied by one peak of an anti-field (co-field) out-of-phase TWDEP propulsion force and electro-rotational torque at the interfacial relaxation frequency. This work completes the classical theory of DEP, which is still widely used by the research community.

In this study, although double-layer polarization on the ideally polarizable surface would make the electric field in the bulk no longer phase-constant around the reciprocal RC time constant $f_{RC} = O(10^3)$ Hz, the TWDEP force field has a negligibly small impact on the dynamic behavior of the binary colloid mixture fed from the channel inlet since charge relaxation frequency at the particle/medium interface is always out of the frequency range that electrochemical ion relaxation dominates in. To this end, we exclude the effect of out-of-phase charging dynamics at the particle surface and thereby mainly focus on the in-phase DEP effect on high-throughput particle separation affected by an electric field gradient.

As shown in Fig. 2, in-phase polarizability of yeast cells (blue dotted lines) and PS microspheres (red solid lines) with respect to the buffer medium, namely, the real part value $\text{Re}(CM)$ of the C-M factor, is calculated as a function of

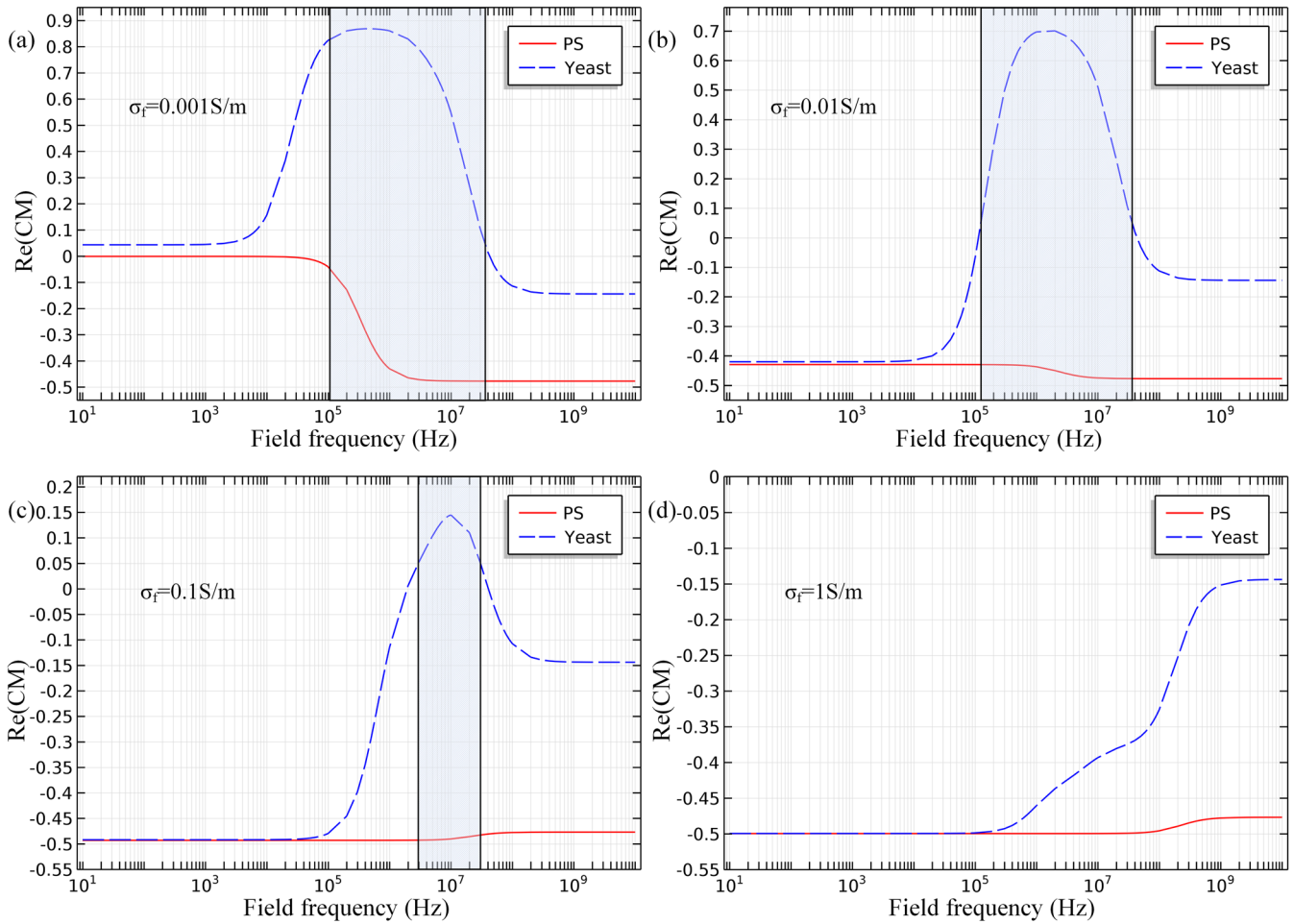


FIG. 2. Effect of ionic conductivity of the buffer medium on in-phase induced polarizability of yeast cells (the blue dotted lines) and latex beads (the red solid lines) in a broad frequency range for distinct liquid conductivities. (a) $\sigma_f = 0.001$ S/m, (b) 0.01 S/m, (c) 0.1 S/m, and (d) 1 S/m.

applied field frequency for distinct liquid conductivities. As the ionic strength increases logarithmically from 0.001 to 1 S/m [Figs. 2(a)–2(d)], the effective frequency band for DEP separation decreases dramatically (the shaded regime), within which the yeasts experience pDEP force and would be captured within the device channels; simultaneously, PS beads undergo nDEP repulsion and would transport with the laminar flow toward channel exit, resulting in successful electrokinetic separation of the binary sample mixture.

As for the polarization trait of bioparticles, on one hand, considering the capacitively charging behavior of the insulating cell membrane, the yeasts are always negatively polarized by the applied AC fields in the low-frequency limit. On the other hand, at high field frequencies, displacement current plays an important role and yeasts experience a nDEP force field once again due to its lower permittivity than the buffer medium. From a physical point of view, however, the conductivity of the inner concentric layer begins to take effect and may make the cells positively polarized in an intermediate frequency range [Figs. 2(a)–2(c)], and a finite conductivity of the inner core of yeasts would make them even less polarizable as the ionic conductivity of liquid suspension continuously rises, as evidenced by a decrease of the maximum value of $\text{Re}(\text{CM})$ of yeasts from 0.9 to 0.15 [Figs. 2(a)–2(c)], while being still positive. Moreover, since the yeasts suffer from nDEP force

fields at the highest medium conductivity of 1 S/m, there are no longer suitable frequencies for achieving the task of separation [Fig. 2(d)].

In stark contrast to the double transition frequencies for cells of multiple shelled structures, the polarization curve of colloidal microspheres is always negative and hence does not possess any critical frequency point for reversing the DEP force polarity (Fig. 2), in view of the non-uniform surface conduction being inversely proportional to the object dimension. Accordingly, taking into consideration a realistic culture condition of biological cells as well as strong DEP force magnitude experienced by micro-entities, a moderate buffer ionic strength 0.01 S/m is chosen in priority for all subsequent analysis to give our microdevice the capability of separating this binary mixture [Fig. 2(b)]. Meanwhile, the range of device operating frequency is confined between 100 kHz and 10 MHz, within which yeast cells and PS beads would feel net electrokinetic forces in opposite directions [the shaded region in Fig. 2(b)].

2. Electrode polarization

Due to a force equilibrium between electrostatic attraction and Brownian diffusion at a solid/liquid interface, a Debye screening layer, within which counter-ions dominates co-ions, would form either naturally due to the native surface charge

chemically adsorbed on the solid surface or compulsively driven by externally applied DC/AC fields. In the current analysis, since AC fields are applied to DE pairs, Coulomb force exerted on the native EDL charge would time average to zero under harmonic actuations. For such, we merely focus on the latter effect of diffuse-charge dynamics, namely, double-layer capacitive charging on ideally polarizable surfaces induced by sinusoidal voltages imposed on the DEs.

In the DC limit, due to the occurrence of relatively complete Debye screening, most of the applied voltage amplitude ($V_D = 30$ V) drops across the IDL at the metal/electrolyte interface [Fig. 3(c)], resulting in rather weak electric field intensity inside the bulk fluid above the conducting surfaces [Fig. 3(a)]. As the imposed field frequency increases and surpasses the inverse RC charge relaxation time for the driving electrode f_{DE}^{RC} , incomplete Debye screening takes place on the DE surface due to electrochemical ion relaxation within the IDL, resulting in appreciable electric field leakage into the suspension medium.

In this way, the value of the overpotential between the DE surface and electrolyte drops sharply for frequencies beyond $f_{DE}^{RC} \approx 50$ Hz [Fig. 3(c)] and the enhanced bulk field intensity resulted from this factor helps polarize the central FE array, giving rise to a single relaxation peak of double-layer induced

charge on each array element around $f = 100$ Hz [the red line in Fig. 3(c)]. With further increase of frequency even exceeding the reciprocal RC time constant for capacitive charging of the floating electrode $f_{FE}^{RC} \approx 500$ Hz, however, double-layer charge relaxation appears on those FEs so that induced zeta potential phasor would diminish at the FE/electrolyte interface.

Accordingly, as we raise the electric field frequency from the DC limit to 10 MHz, the voltage drop across the IDL on DE decays monotonously due to a charge relaxation process. On the contrary, the variation trend of the zeta potential on the conducting surface of each FE element peaks at an intermediate frequency around $f = 100$ Hz and is characterized by a bell-shaped curve [Fig. 3(c)], implying that the degree of electrochemical polarization of FE can be dramatically suppressed once the exciting frequency further deviates from the key frequency.

At low field frequencies, all of the applied voltage drops across the electrical double layer (EDL) adjacent to the driving electrodes (DEs) on both sides, leaving no electric field in the bulk. Accordingly, the FE array cannot be sufficiently polarized, resulting in a weak induced zeta potential at the FE/liquid interface [10 Hz in Fig. 3(c)]. In the high frequency limit, charge relaxation within the Debye layer becomes important, that is, there is not enough time for the counterionic charge

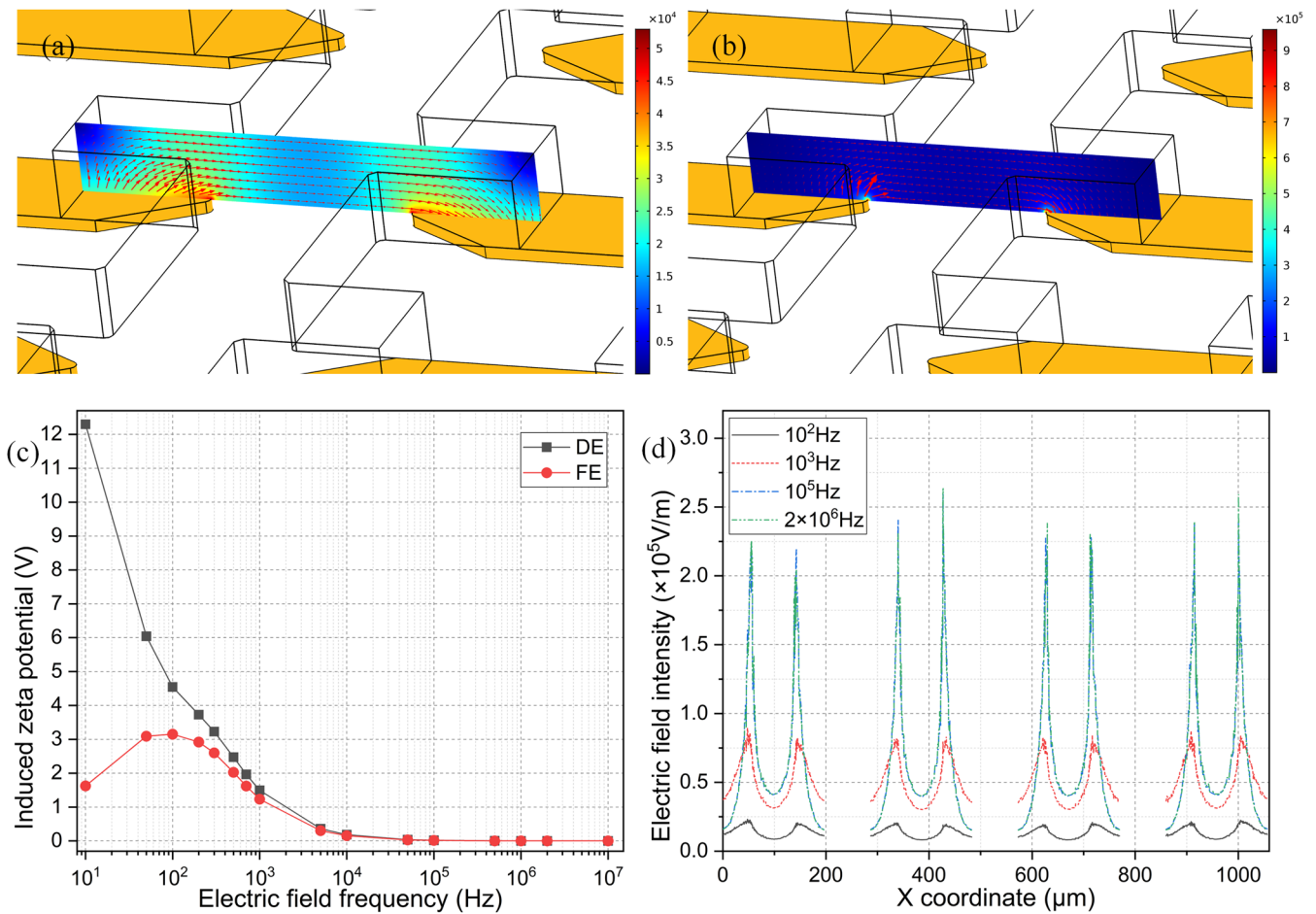


FIG. 3. Simulation results of the electrode polarization effect in the basic device configuration (chip α) under a given driving voltage of $V_D = 30$ V. (a) A surface and arrow plot of the in-plane electric field distribution at $f = 200$ Hz and (b) $f = 1$ MHz in the A-A' cross section passing through the opposing electrode tips within a unit calculation cell (unit: V/m). (c) Frequency-dependence of induced zeta potential phasor across the IDL on DE and FE. (d) Distribution of electric field intensity along the x-axis at a vertical distance of $z = 3$ μ m away from the electrode surface for distinct field frequencies.

cloud to accumulate within the EDL on the ideally polarizable surface in each half cycle of the AC voltage wave, giving rise to a negligible small induced zeta potential once again [$f > 100$ Hz in Fig. 3(c)]. Based on these two aspects, double-layer charging of the FE array is most evident at the key frequency ($f = 100$ Hz), and any deviation of the applied field frequency from this critical point would weaken the phenomenon of electrode polarization.

In this way, electrode polarization on both DEs and FEs has strong but different frequency dependence, which directly affects the distribution of the electric field in the bulk phase. As shown in Fig. 3(d), with an increase of field frequency from 100 Hz to 2 MHz, all the IDLs at the metal/medium interface are more severely short circuited by the displacement current in time-varying fields, namely, the phenomenon of electrochemical ion relaxation. As a result, more electric field lines would penetrate into the fluid domain from the thin Debye layer, which supplies the necessary conduction current to constantly transport the counterionic charge into or out of IDL within each repeating half cycle of a high-frequency AC voltage wave.

It is noteworthy that, as the frequency is elevated, not only is the intensity of the electric field enhanced to great extent within the separation channels but it becomes more non-uniform as well [Fig. 3(d)]. From the perspective of an observer, the electrodes would recover from an insulator in the DC limit [Fig. 3(a)] to its original role of an ideal conductor [Fig. 3(b)] in the high-frequency range with a characteristic distance scale $O(\lambda_D)$ away from the ideally polarizable surface. For such, the normal field component dominates over the tangential counterpart at high field frequencies [Fig. 3(b)], resulting in reinforced field gradients than the low-frequency situation [Fig. 3(a)] where the magnitude of field components in both directions is comparable. Considering the adverse effect of electrode polarization, ideal operating frequency of the microfluidic separation device should be at least no less than 100 kHz; then, the DEP force fields for both kinds of micro-entities can be fully developed.

3. AC-field induced charge electroosmosis

In addition to exerting a negative influence on the electric field distribution, electrochemical polarization at the electrolyte/electrode interface simultaneously induces ICEO fluid motion in the low-frequency limit, which often behaves as a series of micro-vortices streaming above the FE array. As shown in Fig. 4(a), for a repeating unit cell of the calculation space consisting of two nearest ends of a neighboring FE pair, since ICEO is driven by nonlinear Coulomb force within thin IDL at the nanometer scale, the time-averaged flow velocity is the fastest right on the surface of FEs and diminishes at the midchannel in the inter-electrode gap due to the vertical confinement effect from a finite channel height.⁶⁴

Nonlinear electroosmosis on electrodes with the potential fixed by an external powering source is conventionally referred to as ‘‘AC electroosmosis’’ (ACEO), in order to differentiate such effect from ICEO on floating electrodes of a natural inducing potential affected by a background electric field. According to the linear asymptotic analysis by

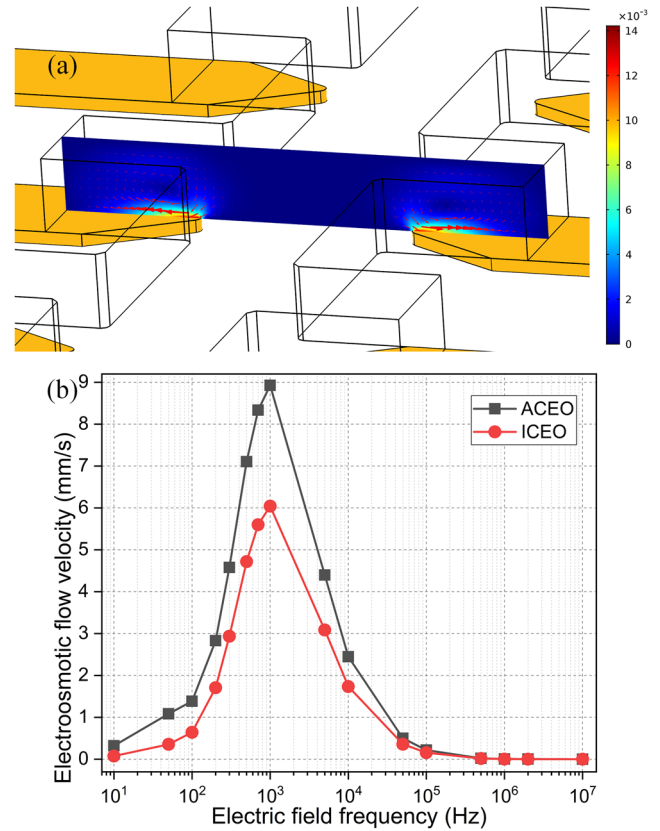


FIG. 4. Effect of ICEO fluid motion in device α . (a) A surface and arrow plot of the in-plane ICEO vortex flow field in the A-A' cross section within a unit cell for $V_D = 30$ V and $f = 300$ Hz (unit: m/s). (b) Frequency-dependence of flow velocity of ACEO on DE and ICEO on the FE array.

González *et al.*,⁶⁵ ACEO is merely important around double-layer dispersion frequency and vanishes at both low (due to screening of bulk electric field) and high (due to charge relaxation) field frequencies. On the contrary, ICEO can survive in either steady DC or low-frequency AC fields, in that the tangential electrical field component acting on the induced ionic charge within IDL is provided by an externally imposed potential gradient, rather than the bipolar FE itself. Even so, both ACEO and ICEO vanish in the DC limit for the current electrode layout regardless of this general physical description [Fig. 4(b)].

The field source and sink that enable the induction of ICEO on each array element arise from the AC voltage signal imposed on the DE pair at both sides. In the numerical calculation, it is taken into consideration that they also experience severe field screening in low frequencies, resulting in insufficient action of the background field intensity on the free ionic charge adjacent to the FE surface. For this reason, as shown in Fig. 4(b), both ACEO on DE and ICEO on the FE array exhibit a single relaxation peak around the inverse RC time scale for capacitive charging of the interfacial impedance $f_{RC} = O(10^2 - 10^3)$ Hz, which is about 3–4 orders of magnitude smaller than the charge relaxation frequency $f_{MW} = \sigma_f / 2\pi\epsilon_f = 2.25$ MHz for the onset of bulk ionic screening. In view of this, we can safely disregard the ICEO flow rotation effect on particle trapping at the ideal separation frequency $f = 2$ MHz [Fig. 4(b)].

4. Smeared structural polarization of the bulk phase

Though the above analysis indicates electrochemical polarization and concurrent ICEO vortex flow field dominate within the range of low field frequencies, both of them do not have any mutual interference with electrokinetic separation using a high exciting frequency. If there is sufficient temperature elevation inside the bulk fluid, however, another kind of electroconvection named ACET will appear above 100 kHz.

The most pioneering research on ACET is the discovery of traveling-wave induced electroconvection [traveling-wave electrothermal (TWET)] by Melcher and Firebaugh.⁶⁶ In their physical model, a temperature gradient is externally imposed across a liquid layer using thin-film resistance heaters; this induces a non-uniform distribution of solution conductivity changing linearly along the channel depth direction. If the liquid is then subjected to a phase-shifted traveling voltage wave orthogonal to the conductivity gradient, a smeared spatial charge is induced inside the bulk phase, as asked by the continuity condition of electric current flow within the fluid domain. These charged ions relax in the liquid to form a traveling wave that lags behind the image surface charge accumulated on the phase-shifted electrode array, which in turn interplays with the imposed complex field to pump the solution at Maxwell-Wagner relaxation frequency of the bulk. For such, TWET exploits the out-of-phase component of induced polarization and has a single relaxation peak at an intermediate frequency where ohm and displacement currents become comparable.

Later, Ramos *et al.*⁴⁸ and Gimsa *et al.*⁴² proposed the general theory of ACET that originates from the interaction of an imposed AC field with its own induced charge in saline solution and coined the term “smeared structural polarization” to depict the diffusive feature of dielectric dispersion of the bulk fluid occurring in ACET, versus the surface-coupled nature of particle DEP where the electric properties are piecewise constant on either side of the phase interface. In this way, although the specific zones of induced polarization are different, ACET and TWET convection (bulk polarization) in electrolyte can be well compared with the conventional in-phase DEP force on latex beads in a field gradient and out-of-phase electrorotation in circularly polarized electric fields (interfacial polarization), respectively, in terms of an identical Maxwell-Wagner polarization mechanism.

As shown in Fig. 5(a), the application of an AC electric field causes non-uniform medium heating due to strong Ohmic current flowing across the conductive solution between neighboring FEs. A local maximum temperature elevation is produced right above the electrode tips, by taking a large *in situ* electric field strength into account. With strong electro-thermal coupling, a symmetric ACET vortex flow field appears in every repeating unit cell within a broad frequency range from 500 kHz [Fig. 5(b)] to 500 MHz [Fig. 5(c)], as characterized by the reciprocal charge relaxation time of bulk electroconvection in a thermal gradient $f_{ACET} = \sigma_f \sqrt{1 - 2\beta/\alpha} / 2\pi\epsilon_f = 7.45 \text{ MHz}$ for a liquid conductivity of 0.01 S/m.

As the exciting frequency is lower than f_{ACET} , since there is sufficient time for net ionic charges to relax inside the bulk phase within each half period of the AC voltage, Coulomb

force in a conductivity gradient drives relatively fast ACET fluid motion in the branching channels [regime II in Fig. 5(e)]. For frequencies well beyond f_{ACET} , free charge density diminishes owing to a relaxation phenomenon and merely dielectric force acting on the polarized bound charge would survive in the high-frequency limit, reducing the ACET flow rate by nearly tenfold [regime III in Fig. 5(e)]. Since the two components of electrothermal body force are opposite to one another, the rolling direction of ACET micro-vortices makes a reversal from being divergent [Fig. 5(b)] to being convergent [Fig. 5(c)] adjacent to electrode tips as electric field frequency passes over f_{ACET} .

Fluid physics of ACET in the current device design is even more complex than the above analysis, in terms of a possible adverse effect of electrode polarization on the induction of smeared spatial charges through simultaneous bulk field screening and suppression of electric heat generation [Fig. 5(d)] below the inverse RC time constant for IDL capacitive charging f_{RC} [regime I in Fig. 5(e)]. As a consequence, flow behavior of electrothermal convection features nonmonotonic and bell-shaped frequency-dependence [Fig. 5(e)], with the velocity magnitude achieving one peak plateau at the intermediate frequency range between $f_{RC} = 0(10^3) \text{ Hz}$ and $f_{ACET} = O(10^6) \text{ Hz}$ where Coulomb force plays an important role. Besides, though the ACET flow velocity still decays above $f = 10^6 \text{ Hz}$ [Fig. 5(e)], the maximum temperature elevation attains a stable highland for $f \geq 10^5 \text{ Hz}$ [Fig. 5(d)]. That is, the decreasing ACET flow velocity with an increase of applied field frequency has no effect on the thermal field. Considering a small thermal Peclet number $Pect = 0.07$ (see the Nomenclature), however, this indeed holds true in the current microfluidic separation device.

Because ACET fluid motion is quite weak, $O(1) \mu\text{m/s}$ under preset parameters for DEP manipulation, it would not exert any negative impact on the separation performance with $E_B = 30 \text{ V/mm}$ and $\sigma_f = 0.01 \text{ S/m}$. Nevertheless, since it is proportional to the fourth-power of electric field intensity and grows linearly with ionic strength, we can arbitrarily enhance the effect of ACET with respect to any other nonlinear electrokinetic phenomena of a second-order voltage dependence (e.g., DEP) by increasing either the voltage amplitude or the solution conductivity, so as to achieve multiple functionalities other than a high-throughput separation required here.

B. Integrated device design for high-throughput DEP separation

Four distinct electrokinetic phenomena, including electrochemical ion relaxation, nonlinear electroosmosis, interfacial polarization, and bulk electroconvection, have been elaborated in Sec. III A. With a reasonable set of experimental parameters (liquid conductivity 0.01 S/m, field frequency around the onset for bulk ionic screening $f = 2 \text{ MHz}$, and moderate field strength $E_B = 30 \text{ V/mm}$), time-averaged DEP motion of colloids dominates over fluid flows driven by EHD mechanisms (i.e., ACET, ACEO, and ICEO). Accordingly, we then develop a highly integrated device design [Fig. 1(b)] for the sake of high-flux DEP separation. There are thirty-two FEs embedded among five branching channels in parallel configuration. Yeast cells and latex beads are suspended in a buffer

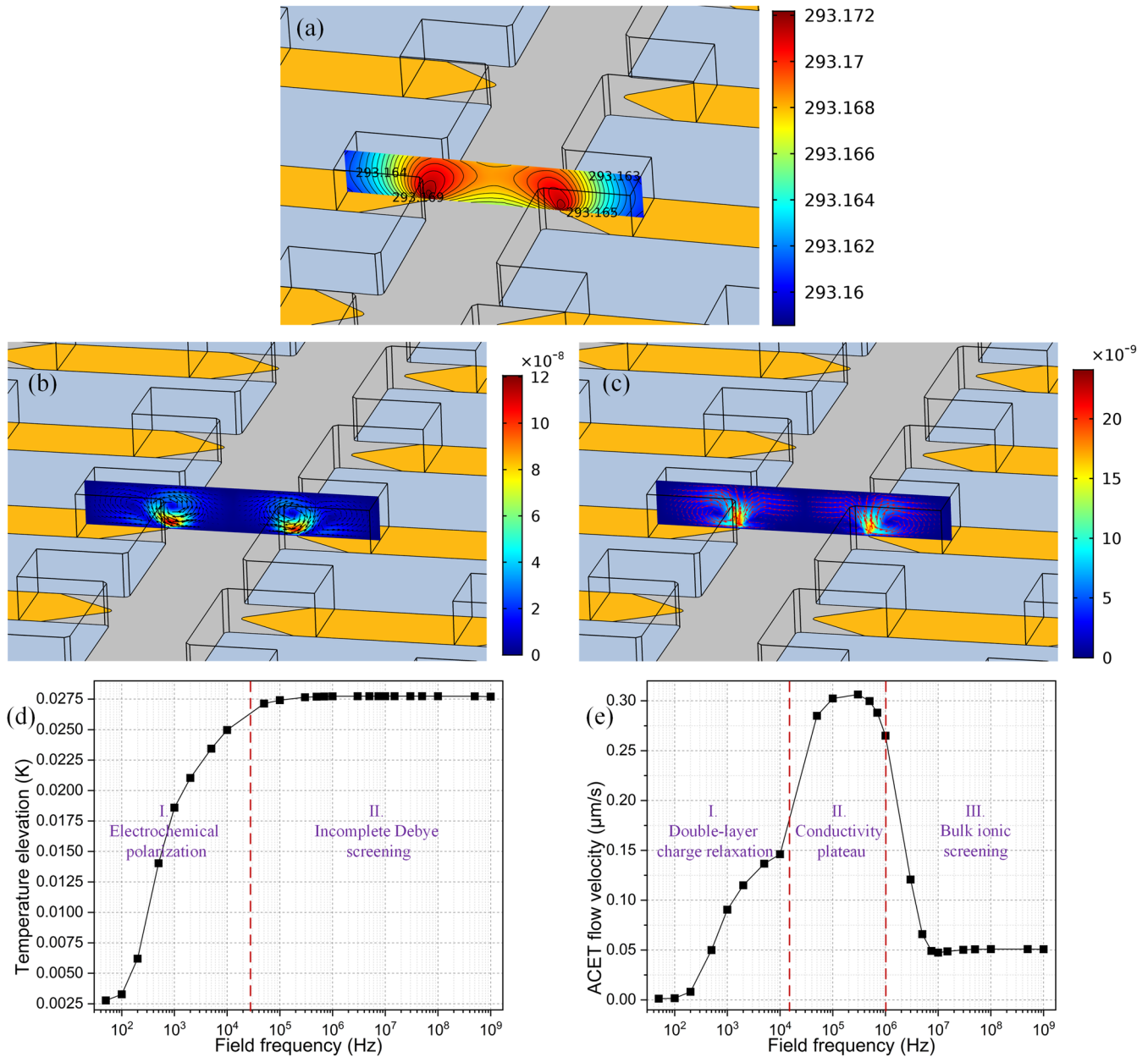


FIG. 5. Effect of induction EHD in device α for $V_D = 30$ V. (a) A surface and contour plot of the temperature field in the A-A' cross section at 500 kHz (unit: K). (b) A surface and arrow plot of ACET whirlpool at 500 kHz and (c) 100 MHz in the A-A' cross section (unit: m/s). (d) Frequency-dependence of maximum temperature elevation within each branching channels. (e) Theoretical prediction of characteristic ACET flow velocity as a function of applied field frequency.

medium with a neutral number density ratio of 1:1 and continuously pumped into the microfabricated fluidic networks from the upstream channel inlet.

1. Distribution of electric field phasor and DEP force fields

On application of an AC signal of $V_D = 60$ V and $f = 2$ MHz, since electrode kinetics has been severely inhibited, a strong electric field gradient is induced inside the suspension medium with incomplete Debye screening. In the horizontal x - y plane with a vertical distance of $z = 3$ μm away from the channel bottom surface [Fig. 6(a)], the potential gradient is unevenly distributed in the transverse direction. Specifically, the electric field intensity reaches a peak value of 400 V/mm in the immediate vicinity of electrode tips, while a

valley point of 20 V/mm in the midchannel is seen [Fig. 6(b)], under the influence of an externally imposed electric field of $E_B = 30$ V/mm.

With larger levitation height from the electrode surface, however, electric field drops dramatically from $z = 3$ μm until reaching $z = 12$ μm , implying a quite limited action area of DEP force fields near the metal electrodes within separation chambers [Figs. 7(b) and 7(d)]. In view of this, the height of the channel remains unchanged at $H = 30$ μm in the integrated design [Fig. 1(b)], with respect to the simple structure for fundamental investigations [Fig. 1(a)]. Then, the separation throughput can be improved by increasing the scale of the other two dimensions (x and y). For instance, we configured more separation channels in the lateral direction (x) and placed more bipolar GE (gate electrode) in the pockets along

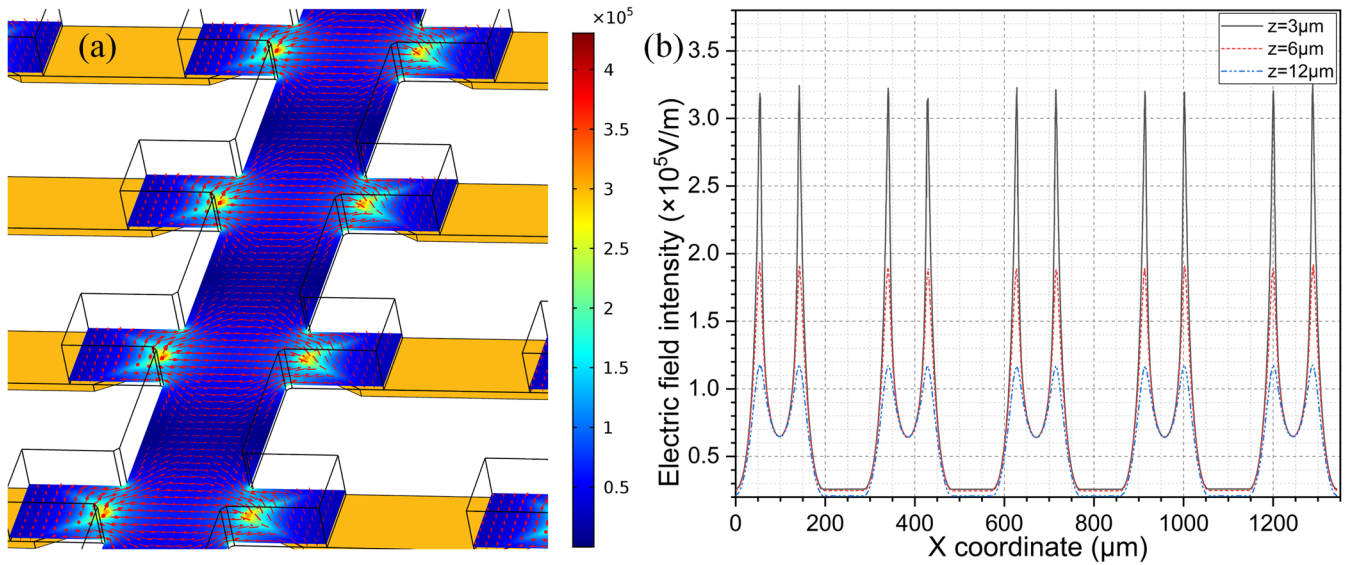


FIG. 6. Analysis of the electric field distribution in the highly integrated device architecture having a 5×8 FE array (device β) at $V_D = 60 \text{ V}$ and $f = 2 \text{ MHz}$. (a) A surface and arrow plot of the AC electric field (unit: V/m) in a horizontal plane with vertical distance $z = 3 \mu\text{m}$ away from the electrode surface (B-B' cross section). (b) Electric field strength along the channel width direction at different height z right above the electrode centerline.

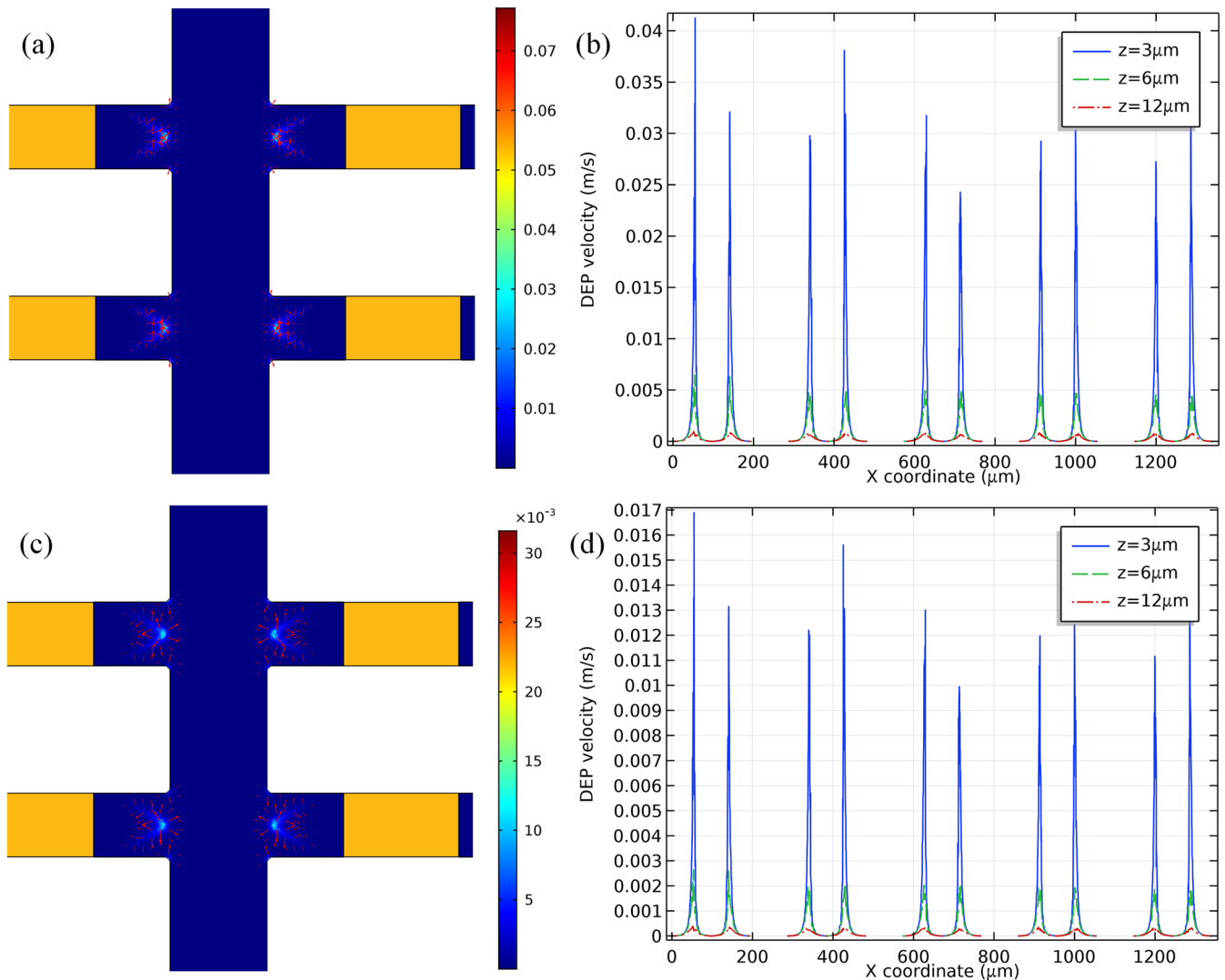


FIG. 7. Characterization of the DEP effect in device β at $V_D = 60 \text{ V}$ and $f = 2 \text{ MHz}$. (a) A surface and arrow plot of the pDEP velocity field of yeast cells in the B-B' cross section (unit: m/s). (b) Magnitude of DEP velocity of yeast cells as a function of the X coordinate at different levitation height z . (c) A surface and arrow plot of the nDEP velocity field of PS colloids in the B-B' cross section (unit: m/s). (d) Magnitude of DEP velocity of latex beads as a function of the X coordinate at different levitation height z .

the length direction of each branch (y) to extend the actuation range of DEP force fields.

Since there is strong field gradient near electrode surfaces as well as the sharp pocket/channel junctions, pDEP force acting on yeast cells tends to capture them in these two regions [Fig. 7(a)]. On the contrary, latex beads fed from the inlet are well repelled by nDEP to the channel centerline [Fig. 7(c)] and then transport downstream together with incoming pressure-driven flow, resulting in feasible electrokinetic separation.

2. Laminar streaming

For generating high-throughput, we introduced five parallel branching channels. As shown in Fig. 8(a), fluid motion exhibits a laminar state, indicating that the axial pressure-driven flow for liquid injection is several orders of magnitude stronger than turbulent electroconvection in the transverse direction, namely, ICEO and ACET can be safely disregarded

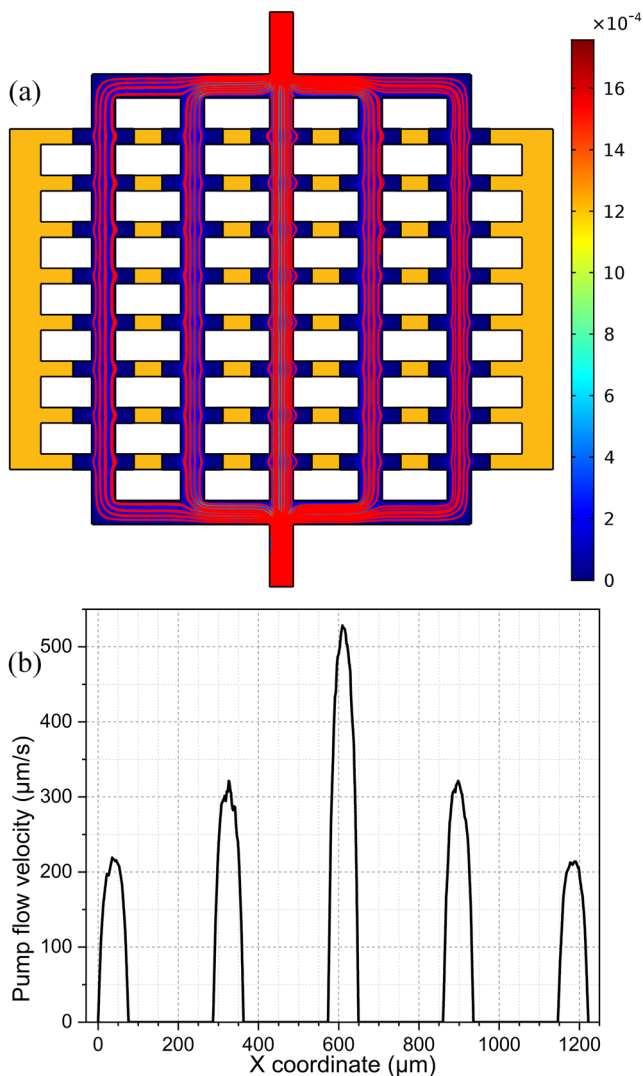


FIG. 8. Analysis of fluid flows driven by a pressure difference externally imposed across the two opposite electrolytic ports at a given inlet flow rate of $u_0 = 1$ mm/s. (a) A surface and streamline plot of the incoming laminar streams (unit: m/s) in the middle plane ($z = H/2 = 15 \mu\text{m}$). (b) The velocity profile of the Poiseuille flow along the width direction of five sequential branching channels.

in this situation, simplifying the flow field analysis to a great extent.

Though the laminar streamlines within each fluidic channel are of a similar Poiseuille flow profile, the induced flow rate is unequally distributed along the x -direction. Colloids pass through the central branch with the quickest speed, while the slowest fluid motion appears in the two side branches [Fig. 8(b)]. The reason behind this consists in an asymmetric bifurcating scheme employed upstream just before the sample particles enter these branching channels [Fig. 8(a)]. This causes a dispersive output-flux along the channel width direction, which holds promise to impact a wide range of

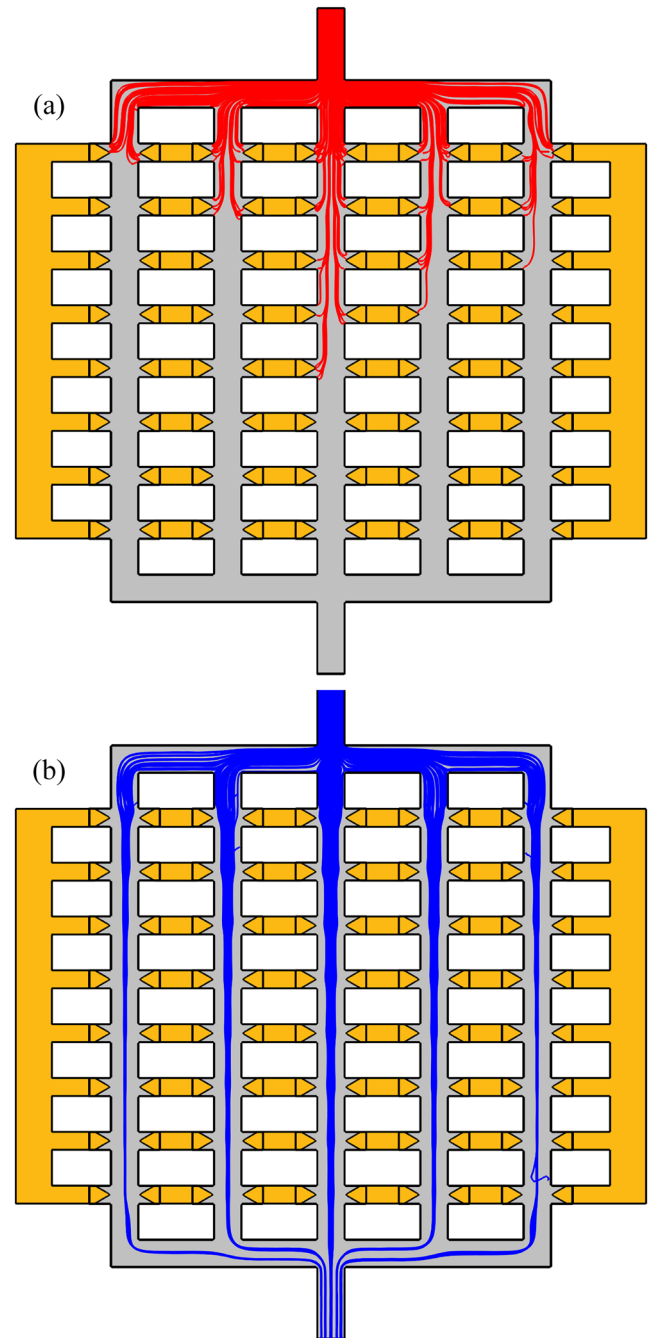


FIG. 9. Calculation result of the resultant particle velocity from DEP, laminar stream, ACET, ICEO, and buoyancy. (a) A streamline plot of yeast cells' velocity field in the integrated device design. (b) A streamline plot of latex beads' velocity field within the fluid.

on-chip applications that need to produce a concentration gradient.

3. Motion trajectories of binary colloid mixture during DEP separation

By superimposing the effects of DEP, laminar stream, and sedimentation all together, the resultant velocity field of yeasts

and latex beads is obtained and displayed as streamlines plotted in Figs. 9(a) and 9(b), respectively. On one hand, PS colloids are squeezed by nDEP to form thin streams in the midchannel, then flow through the fluidic networks, and finally exit from the channel outlet as five co-flowing slim particle beams [Fig. 9(b)]. On the other hand, flow streamlines of yeasts experiencing pDEP move towards either the electrode tips or the pocket/channel junctions [Fig. 9(a)].

Distinct dynamic behaviors of the binary sample mixture enable successful DEP separation under a large inlet flow rate $u_0 = 1$ mm/s, as demonstrated by the numerical prediction of motion trajectories of incoming colloids shown in Fig. 10 (multimedia view). After they have entered the channel inlet for 10 s, the dielectric microspheres flowing through the side branches move over a distance about 2.2 mm [the leftmost and rightmost blue particle beams in Fig. 10(a) (multimedia view)], which is equivalent to a time-averaged speed of $220 \mu\text{m/s}$ [Fig. 8(b)], while the central three streams of PS beads have already discharged from the channel outlet in terms of larger translational velocities within $300\text{--}500 \mu\text{m/s}$ [Fig. 8(b)]. At $t = 30$ s, the minimum physical displacement of incoming particle samples has theoretically attained 6.6 mm so that the five co-flowing thin streams consisting of latex spheres are continuously advected downstream at the exit plane [Fig. 10(b) (multimedia view)]. In the meantime, a large amount of yeast cells [red spheres in Fig. 10 (multimedia view)] are irreversibly captured adjacent to the ideally polarizable surface of the FE array configured in parallel along the channel length direction, and almost no yeasts move into the exit on account of strong DEP attraction within these branching channels [Fig. 10(b) (multimedia view)]. In this way, high-throughput electrokinetic separation of the binary particle mixture characterized by opposite in-phase polarity is realizable with a large-scale FE array embedded in microfabricated fluidic networks.

IV. CONCLUSION

To summarize, we have presented the results from both a physical perspective and simulation analysis to account for high-throughput DEP separation of the binary colloid mixture in a microdevice embedding a large-scale bipolar electrode array. Four nonlinear electrokinetic phenomena have been well distinguished, including electrode polarization, ICEO, ACET, and DEP, which are originated by diffuse charge dynamics, electrochemical ion relaxation, smeared dielectric dispersion, and Maxwell-Wagner interfacial polarization in externally applied AC fields, respectively. Through an in-depth investigation of basic physical mechanisms, it is revealed that EHD fluid motion manifests as transversal turbulent streamlines, and the resultant rotational dynamics would possibly affect the motion trajectory of incoming colloidal particles adjacent to the conducting surface of each array unit, whose opposite end is in direct contact with the saline solution, while the central section is tightly covered by insulating channel walls. Based on a reasonable selection of electric field parameters with the sovereign DEP effect, however, convective mixing due to the action of EHD flow diminishes; therefore, two types of incoming particles with opposite in-phase polarity can be smoothly

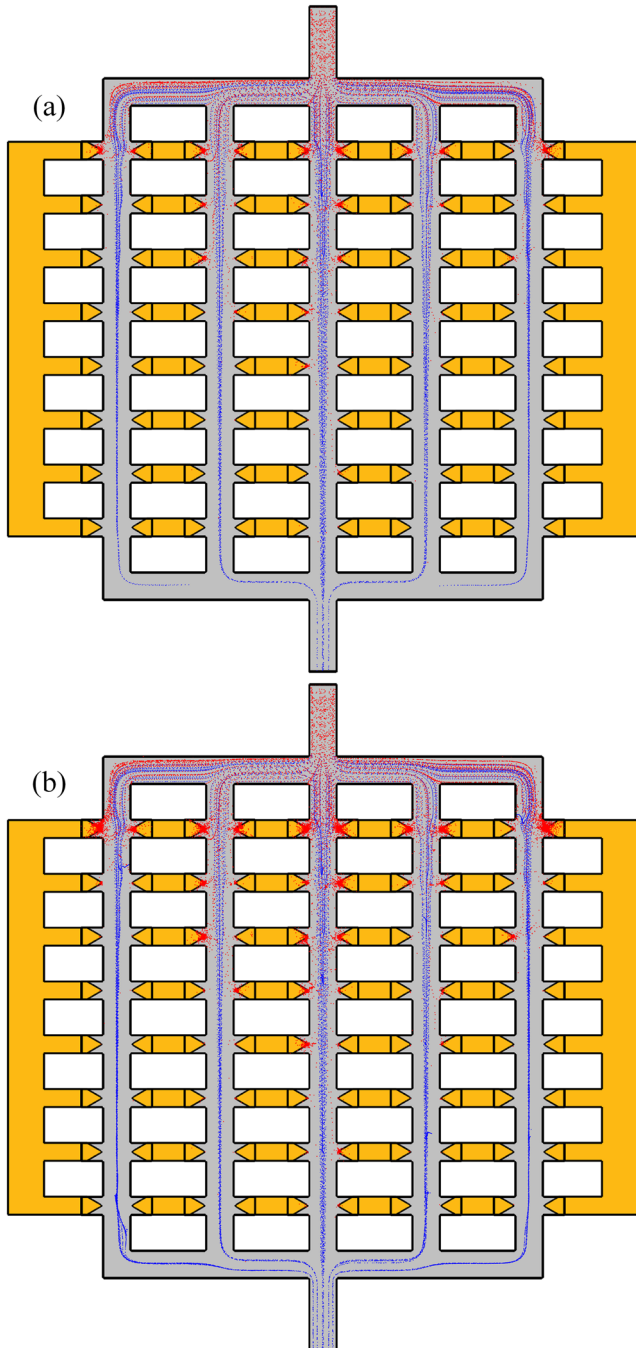


FIG. 10. Numerical prediction of motion trajectories of the binary colloid mixture injected from channel inlet at $t = 0$, with the red and blue dots denoting yeast cells and PS colloids, respectively. (a) Simulation result at $t = 10$ s and (b) $t = 30$ s. It is worth mentioning that the motion trajectory of latex beads is eventually directed to the downstream outlet in the form of five co-flowing thin particle streams due to the action of nDEP repulsion, while more and more yeast cells are collected around the electrode tips and pocket corners by pDEP attraction as time elapses. Multimedia view: <https://doi.org/10.1063/1.5054800.1>

separated in a highly integrated device architecture, where the admissible throughput is in commensurate with the specific scale of the central FE array. Further work on this subject may include the study of utilizing more complex layouts of nonplanar FEs for achieving multiple functionalities in a single chip, such as sample preparation, concentration, detection, and characterization. The results of the current analysis demonstrate the general merits of the application of bipolar electrodes in typical microsystems, in terms of enabling scalable, high-flux electrokinetic platforms by imparting a high degree of freedom flexibility in device design that is impossible with traditional electrode structures. We firmly believe that electrokinetic phenomena induced around FE in an electrolyte environment are going to inspire interdisciplinary research focused on condensed matter, analytical chemistry, and on-chip bioassay in the near future.

ACKNOWLEDGMENTS

This project was financially supported by the National Natural Science Foundation of China (Nos. 11672095, 11702035, and 11702075), Opening Fund of State Key Laboratory of Nonlinear Mechanics, Chang'an University Fundamental Research Funds for the Central Universities (Nos. 310832171008, 300102328201, and 300102328501), Shaanxi kefa (2018) No. 9 key industrial innovation chain (group)-industrial field (Nos. 2018ZDCXL-GY-05-04 and 2018ZDCXL-GY-05-07-02), and Self-Planned Task (SKLRS201803B) of State Key Laboratory of Robotics and System (HIT).

- ¹M. Y. Han, K. H. Park, and S. Dockko, *Particle Separation Technologies for Wastewater Treatment* (IWA Publishing, 2007), ISBN: 1843395665.
- ²B. D. Plouffe, "Magnetic particle based microfluidic separation of cancer cells from whole blood for applications in diagnostic medicine," Ph.D. dissertation (Northeastern University, 2011).
- ³X. Zhang, "Development of a microengineered approach for quantitative assessment of intercellular communication in cell doublets and microscale tissue models," Ph.D. dissertation (The Ohio State University, 2015).
- ⁴H. Tani, K. Maehana, and T. Kamidate, "Chip-based bioassay using bacterial sensor strains immobilized in three-dimensional microfluidic network," *Anal. Chem.* **76**, 6693 (2004).
- ⁵A. M. Leshansky, A. Bransky, N. Korin, and U. Dinnar, "Tunable nonlinear viscoelastic 'focusing' in a microfluidic device," *Phys. Rev. Lett.* **98**, 234501 (2007).
- ⁶X. Ding, S.-C. S. Lin, B. Kiraly, H. Yue, S. Li, I.-K. Chiang, J. Shi, S. J. Benkovic, and T. J. Huang, "On-chip manipulation of single microparticles, cells, and organisms using surface acoustic waves," *Proc. Natl. Acad. Sci. U. S. A.* **109**, 11105 (2012).
- ⁷J. Zeng, Y. Deng, P. Vedantam, T. R. Tzeng, and X. Xuan, "Magnetic separation of particles and cells in ferrofluid flow through a straight microchannel using two offset magnets," *J. Magn. Magn. Mater.* **346**, 118 (2013).
- ⁸H. J. Keh and Y. Wei, "Diffusiophoretic mobility of spherical particles at low potential and arbitrary double-layer thickness," *Langmuir* **16**, 5289 (2000).
- ⁹S. Shin, O. Shardt, P. B. Warren, and H. A. Stone, "Membraneless water filtration using CO₂," *Nat. Commun.* **8**, 15181 (2017).
- ¹⁰H. Lee, J. Kim, J. Yang, S. W. Seo, and S. J. Kim, "Diffusiophoretic exclusion of colloidal particles for continuous water purification," *Lab Chip* **18**, 1713 (2018).
- ¹¹D. Li, *Electrokinetics in Microfluidics* (Academic Press, 2004).
- ¹²W. Liu, Y. Ren, Y. Tao, B. Yao, N. Liu, and Q. Wu, "A universal design of field-effect-tunable microfluidic ion diode based on a gating cation-exchange nanoporous membrane," *Phys. Fluids* **29**, 112001 (2017).
- ¹³S. Park and G. Yossifon, "Electrothermal based active control of ion transport in a microfluidic device with an ion-permeable membrane," *Nanoscale* **10**, 11633 (2018).
- ¹⁴A. Esmaeeli, "Dielectrophoretic- and electrohydrodynamic-driven translational motion of a liquid column in transverse electric fields," *Phys. Fluids* **28**, 073306 (2016).
- ¹⁵Z. Liu, D. Li, Y. Song, X. Pan, D. Li, and X. Xuan, "Surface-conduction enhanced dielectrophoretic-like particle migration in electric-field driven fluid flow through a straight rectangular microchannel," *Phys. Fluids* **29**, 102001 (2017).
- ¹⁶S. Mandal, S. Chakrabarti, and S. Chakraborty, "Effect of nonuniform electric field on the electrohydrodynamic motion of a drop in Poiseuille flow," *Phys. Fluids* **29**, 052006 (2017).
- ¹⁷S. Santra, S. Mandal, and S. Chakraborty, "Electrohydrodynamics of confined two-dimensional liquid droplets in uniform electric field," *Phys. Fluids* **30**, 062003 (2018).
- ¹⁸C. Kang, A. Meyer, H. N. Yoshikawa, and I. Mutabazi, "Numerical simulation of circular Couette flow under a radial thermo-electric body force," *Phys. Fluids* **29**, 114105 (2017).
- ¹⁹C. Church, J. Zhu, J. Nieto, G. Ketten, E. Ibarra, and X. Xuan, "Continuous particle separation in a serpentine microchannel via negative and positive dielectrophoretic focusing," *J. Micromech. Microeng.* **20**, 065011 (2010).
- ²⁰C. Church, J. Zhu, G. Wang, T.-R. J. Tzeng, and X. Xuan, "Electrokinetic focusing and filtration of cells in a serpentine microchannel," *Biomicrofluidics* **3**, 044109 (2009).
- ²¹B. Weis Goldstein and T. Miloh, "3D controlled electrorotation of conducting tri-axial ellipsoidal nanoparticles," *Phys. Fluids* **29**, 052008 (2017).
- ²²A. M. Boymelgreen, T. Balli, T. Miloh, and G. Yossifon, "Active colloids as mobile microelectrodes for unified label-free selective cargo transport," *Nat. Commun.* **9**(1), 760 (2018).
- ²³S. Mandal and S. Chakraborty, "Influence of interfacial viscosity on the dielectrophoresis of drops," *Phys. Fluids* **29**, 052002 (2017).
- ²⁴S. Mandal, A. Bandopadhyay, and S. Chakraborty, "Dielectrophoresis of a surfactant-laden viscous drop," *Phys. Fluids* **28**, 062006 (2016).
- ²⁵M. Li and R. K. Anand, "High-throughput selective capture of single circulating tumor cells by dielectrophoresis at a wireless electrode array," *J. Am. Chem. Soc.* **139**, 8950 (2017).
- ²⁶Y. K. Ren, D. Morganti, H. Y. Jiang, A. Ramos, and H. Morgan, "Electrorotation of metallic microspheres," *Langmuir* **27**, 2128 (2011).
- ²⁷P. García-Sánchez, Y. Ren, J. J. Arcenegui, H. Morgan, and A. Ramos, "Alternating current electrokinetic properties of gold-coated microspheres," *Langmuir* **28**, 13861 (2012).
- ²⁸N. Lewpiriyawong, K. Kandaswamy, C. Yang, V. Ivanov, and R. Stocker, "Microfluidic characterization and continuous separation of cells and particles using conducting poly (dimethyl siloxane) electrode induced alternating current-dielectrophoresis," *Anal. Chem.* **83**, 9579 (2011).
- ²⁹A. Valero, T. Braschler, N. Demierre, and P. Renaud, "A miniaturized continuous dielectrophoretic cell sorter and its applications," *Biomicrofluidics* **4**, 022807 (2010).
- ³⁰C. Iiescu, G. Tresset, and G. Xu, "Continuous field-flow separation of particle populations in a dielectrophoretic chip with three dimensional electrodes," *Appl. Phys. Lett.* **90**, 234104 (2007).
- ³¹J. Gimsa, "A comprehensive approach to electro-orientation, electrodeformation, dielectrophoresis, and electrorotation of ellipsoidal particles and biological cells," *Bioelectrochemistry* **54**, 23 (2001).
- ³²C.-P. Jen and W.-F. Chen, "An insulator-based dielectrophoretic microdevice for the simultaneous filtration and focusing of biological cells," *Biomicrofluidics* **5**, 044105 (2011).
- ³³R. Pethig, "Review Article—Dielectrophoresis: Status of the theory, technology, and applications," *Biomicrofluidics* **4**, 022811 (2010).
- ³⁴M. Z. Bazant and Y. Ben, "Theoretical prediction of fast 3D AC electroosmotic pumps," *Lab Chip* **6**, 1455 (2006).
- ³⁵N. G. Green, A. Ramos, A. Gonzalez, H. Morgan, and A. Castellanos, "Fluid flow induced by nonuniform ac electric fields in electrolytes on microelectrodes. III. Observation of streamlines and numerical simulation," *Phys. Rev. E* **66**, 026305 (2002).
- ³⁶A. Ramos, A. González, P. García-Sánchez, and A. Castellanos, "A linear analysis of the effect of Faradaic currents on traveling-wave electroosmosis," *J. Colloid Interface Sci.* **309**, 323 (2007).
- ³⁷C. L. Zhao and C. Yang, "AC field induced-charge electroosmosis over leaky dielectric blocks embedded in a microchannel," *Electrophoresis* **32**, 629 (2011).
- ³⁸Y. Eckstein, G. Yossifon, A. Seifert, and T. Miloh, "Nonlinear electrokinetic phenomena around nearly insulated sharp tips in microflows," *J. Colloid Interface Sci.* **338**, 243 (2009).
- ³⁹O. Schnitzer, I. Frankel, and E. Yariv, "Electrokinetic flows about conducting drops," *J. Fluid Mech.* **722**, 394 (2013).

- ⁴⁰O. Schnitzer and E. Yariv, "Induced-charge electro-osmosis beyond weak fields," *Phys. Rev. E* **86**, 061506 (2012).
- ⁴¹G. Yossifon, I. Frankel, and T. Miloh, "On electro-osmotic flows through microchannel junctions," *Phys. Fluids* **18**, 117108 (2006).
- ⁴²J. Gimsa, M. Stubbe, and U. Gimsa, "A short tutorial contribution to impedance and AC-electrokinetic characterization and manipulation of cells and media: Are electric methods more versatile than acoustic and laser methods?," *J. Electr. Bioimpedance* **5**, 74 (2014).
- ⁴³A. González, A. Ramos, H. Morgan, N. G. Green, and A. Castellanos, "Electrothermal flows generated by alternating and rotating electric fields in microsystems," *J. Fluid Mech.* **564**, 415 (2006).
- ⁴⁴A. Salari, M. Navi, and C. Dalton, "A novel alternating current multiple array electrothermal micropump for lab-on-a-chip applications," *Biomicrofluidics* **9**, 014113 (2015).
- ⁴⁵S. J. Williams, "Enhanced electrothermal pumping with thin film resistive heaters," *Electrophoresis* **34**, 1400 (2013).
- ⁴⁶M. Stubbe and J. Gimsa, "A short review on AC electro-thermal micropumps based on smeared structural polarizations in the presence of a temperature gradient," *Colloids Surf., A* **376**, 97 (2011).
- ⁴⁷A. Castellanos, A. Ramos, A. Gonzalez, N. G. Green, and H. Morgan, "Electrohydrodynamics and dielectrophoresis in microsystems: Scaling laws," *J. Phys. D: Appl. Phys.* **36**, 2584 (2003).
- ⁴⁸A. Ramos, H. Morgan, N. G. Green, and A. Castellanos, "AC electrokinetics: A review of forces in microelectrode structures," *J. Phys. D: Appl. Phys.* **31**, 2338 (1998).
- ⁴⁹F. C. Leinweber, J. C. T. Eijkel, J. G. Bower, and A. van den Berg, "Continuous flow microfluidic demixing of electrolytes by induced charge electrokinetics in structured electrode arrays," *Anal. Chem.* **78**, 1425 (2006).
- ⁵⁰M. Z. Bazant and T. M. Squires, "Induced-charge electrokinetic phenomena: Theory and microfluidic applications," *Phys. Rev. Lett.* **92**, 066101 (2004).
- ⁵¹E. Sheridan, D. Hlushkou, K. N. Knust, U. Tallarek, and R. M. Crooks, "Enrichment of cations via bipolar electrode focusing," *Anal. Chem.* **84**, 7393 (2012).
- ⁵²Y. Ren, W. Liu, Z. Wang, and Y. Tao, "Induced-charge electrokinetics in rotating electric fields: A linear asymptotic analysis," *Phys. Fluids* **30**, 062006 (2018).
- ⁵³W. Liu, J. Shao, Y. Jia, Y. Tao, Y. Ding, H. Jiang, and Y. Ren, "Trapping and chaining self-assembly of colloidal polystyrene particles over a floating electrode by using combined induced-charge electroosmosis and attractive dipole-dipole interactions," *Soft Matter* **11**, 8105 (2015).
- ⁵⁴Y. Ren, X. Liu, W. Liu, Y. Tao, Y. Jia, L. Hou, W. Li, and H. Jiang, "Flexible particle flow-focusing in microchannel driven by droplet-directed induced-charge electroosmosis," *Electrophoresis* **39**, 597 (2018).
- ⁵⁵X. Xuan, B. Xu, D. Sinton, and D. Li, "Electroosmotic flow with Joule heating effects," *Lab Chip* **4**, 230 (2004).
- ⁵⁶W. Liu, Y. Ren, Y. Tao, Y. Li, and X. Chen, "Controllable rotating behavior of individual dielectric microrod in a rotating electric field," *Electrophoresis* **38**, 1427 (2017).
- ⁵⁷X. Chen, Y. Ren, W. Liu, X. Feng, Y. Jia, Y. Tao, and H. Jiang, "A simplified microfluidic device for particle separation with two consecutive steps: Induced charge electro-osmotic prefocusing and dielectrophoretic separation," *Anal. Chem.* **89**, 9583 (2017).
- ⁵⁸T. B. Jones, *Electromechanics of Particles* (Cambridge University Press, 2005).
- ⁵⁹B. D. Iverson, L. Cremaschi, and S. V. Garimella, "Effects of discrete-electrode configuration on traveling-wave electrohydrodynamic pumping," *Microfluid. Nanofluid.* **6**, 221 (2009).
- ⁶⁰W. Liu, Y. Ren, Y. Tao, X. Chen, B. Yao, M. Hui, and L. Bai, "Control of two-phase flow in microfluidics using out-of-phase electroconvective streaming," *Phys. Fluids* **29**, 112002 (2017).
- ⁶¹J. R. Melcher, "Traveling-wave induced electroconvection," *Phys. Fluids* **9**, 1548 (1966).
- ⁶²H. A. Pohl, *Dielectrophoresis: The Behavior of Neutral Matter in Nonuniform Electric Fields* (Cambridge University Press, 1978).
- ⁶³X. Wang, X. B. Wang, and P. R. C. Gascoyne, "General expressions for dielectrophoretic force and electrorotational torque derived using the Maxwell stress tensor method," *J. Electrostat.* **39**, 277 (1997).
- ⁶⁴Y. Tao, Y. Ren, W. Liu, Y. Wu, Y. Jia, Q. Lang, and H. Jiang, "Enhanced particle trapping performance of induced charge electroosmosis," *Electrophoresis* **37**, 1326 (2016).
- ⁶⁵A. González, A. Ramos, N. G. Green, A. Castellanos, and H. Morgan, "Fluid flow induced by nonuniform ac electric fields in electrolytes on microelectrodes. II. A linear double-layer analysis," *Phys. Rev. E* **61**, 4019 (2000).
- ⁶⁶J. R. Melcher and M. S. Firebaugh, "Traveling-wave bulk electroconvection induced across a temperature gradient," *Phys. Fluids* **10**, 1178 (1967).